



# High Temperature Lightweight Self-Healing Ceramic Composites for Aircraft Engine Applications

*S.V. Raj*

*Glenn Research Center, Cleveland, Ohio*

*M. Singh and R.T. Bhatt*

*Ohio Aerospace Institute, Brook Park, Ohio*

## NASA STI Program . . . in Profile

Since its founding, NASA has been dedicated to the advancement of aeronautics and space science. The NASA Scientific and Technical Information (STI) program plays a key part in helping NASA maintain this important role.

The NASA STI Program operates under the auspices of the Agency Chief Information Officer. It collects, organizes, provides for archiving, and disseminates NASA's STI. The NASA STI program provides access to the NASA Aeronautics and Space Database and its public interface, the NASA Technical Reports Server, thus providing one of the largest collections of aeronautical and space science STI in the world. Results are published in both non-NASA channels and by NASA in the NASA STI Report Series, which includes the following report types:

- **TECHNICAL PUBLICATION.** Reports of completed research or a major significant phase of research that present the results of NASA programs and include extensive data or theoretical analysis. Includes compilations of significant scientific and technical data and information deemed to be of continuing reference value. NASA counterpart of peer-reviewed formal professional papers but has less stringent limitations on manuscript length and extent of graphic presentations.
- **TECHNICAL MEMORANDUM.** Scientific and technical findings that are preliminary or of specialized interest, e.g., quick release reports, working papers, and bibliographies that contain minimal annotation. Does not contain extensive analysis.
- **CONTRACTOR REPORT.** Scientific and technical findings by NASA-sponsored contractors and grantees.

- **CONFERENCE PUBLICATION.** Collected papers from scientific and technical conferences, symposia, seminars, or other meetings sponsored or cosponsored by NASA.
- **SPECIAL PUBLICATION.** Scientific, technical, or historical information from NASA programs, projects, and missions, often concerned with subjects having substantial public interest.
- **TECHNICAL TRANSLATION.** English-language translations of foreign scientific and technical material pertinent to NASA's mission.

Specialized services also include creating custom thesauri, building customized databases, organizing and publishing research results.

For more information about the NASA STI program, see the following:

- Access the NASA STI program home page at <http://www.sti.nasa.gov>
- E-mail your question to [help@sti.nasa.gov](mailto:help@sti.nasa.gov)
- Fax your question to the NASA STI Information Desk at 443-757-5803
- Phone the NASA STI Information Desk at 443-757-5802
- Write to:  
STI Information Desk  
NASA Center for AeroSpace Information  
7115 Standard Drive  
Hanover, MD 21076-1320



# High Temperature Lightweight Self-Healing Ceramic Composites for Aircraft Engine Applications

*S.V. Raj*

*Glenn Research Center, Cleveland, Ohio*

*M. Singh and R.T. Bhatt*

*Ohio Aerospace Institute, Brook Park, Ohio*

National Aeronautics and  
Space Administration

Glenn Research Center  
Cleveland, Ohio 44135

## Acknowledgments

The authors thank Mr. Robert Angus, Mr. Raymond Babuder, Mr. Ralph Pawlik, Mr. Ronald Phillips and Mr. Daniel Gorican for their assistance throughout the course of this research. This research was supported by ARMD Seedling Fund Phases I and II and this is gratefully acknowledged.

Trade names and trademarks are used in this report for identification only. Their usage does not constitute an official endorsement, either expressed or implied, by the National Aeronautics and Space Administration.

*Level of Review:* This material has been technically reviewed by technical management.

Available from

NASA Center for Aerospace Information  
7115 Standard Drive  
Hanover, MD 21076-1320

National Technical Information Service  
5301 Shawnee Road  
Alexandria, VA 22312

Available electronically at <http://www.sti.nasa.gov>



# High Temperature Lightweight Self-Healing Ceramic Composites for Aircraft Engine Applications

S.V. Raj  
National Aeronautics and Space Administration  
Glenn Research Center  
Cleveland, Ohio 44135

M. Singh and R.V.Bhatt  
Ohio Aerospace Institute  
Brook Park, Ohio 44142

## Abstract

The present research effort was undertaken to develop a new generation of SiC fiber-reinforced engineered matrix composites (EMCs) with sufficient high temperature plasticity to reduce crack propagation and self-healing capabilities to fill surface-connected cracks to prevent the oxygen ingress to the fibers. A matrix engineered with these capabilities is expected to increase the load bearing capabilities of SiC/SiC CMCs at high temperatures. Several matrix compositions were designed to match the coefficient of thermal expansion (CTE) of the SiC fibers using a rule of mixture (ROM) approach. The CTE values of these matrices were determined and it was demonstrated that they were generally in good agreement with that of monolithic SiC between room temperature and 1525 K. The parameters to hot press the powders were optimized, and specimens were fabricated for determining bend strength, CTE, oxidation and microstructural characteristics of the engineered matrices. The oxidation tests revealed that some of the matrices exhibited catastrophic oxidation, and therefore, these were eliminated from further consideration. Two promising compositions were down selected based on these results for further development. Four-point bend tests were conducted on these two promising matrices between room temperature and 1698 K. Although these matrices were brittle and failed at low stresses at room temperature, they exhibited high temperature ductility and higher stresses at the higher temperatures. The effects of different additives on the self-healing capabilities of these matrices were investigated. The results of preliminary studies conducted to slurry and melt infiltration trials with CrSi<sub>2</sub> are described.

## 1.0 Introduction

Nickel-based superalloys have been successfully used in aircraft engines as blades, combustor liners and vanes for several decades [1]. The use of reliable, high temperature, lightweight materials in the manufacture of aircraft engines is expected to result in lower fossil and bio-fuel consumption, thereby leading to cost savings and lower carbon emissions due to air travel. Designing these hot sections of gas turbine engines with lighter weight silicon carbide fiber-reinforced silicon carbide (SiC/SiC) ceramic matrix composites (CMCs) allows them to operate at higher temperatures and higher pressure ratios with reduced cooling air while leading to lower fuel burn and reduced CO<sub>2</sub> emissions [2,3,4]. As a result, a considerable amount of research has been conducted over the last three decades to develop SiC/SiC CMC technology for aerospace applications [5,6,7,8]. Thus, the technology has matured sufficiently that most major aircraft engine companies in the United States and Europe plan to introduce SiC/SiC CMCs in their next generation aircraft engines [9].

Currently, there are four broad methods for fabricating silicon carbide-based CMCs depending on the matrix processing methods: (a) Melt infiltration (MI), (b) Chemical Vapor Infiltration (CVI), (c) Polymer Infiltration and Pyrolysis (PIP), and (d) Hot Pressing (HP) of SiC powders with additives [8]. In all CMC manufacturing, the starting material is a one-dimensional (1-D) SiC fiber tow, a two-dimensional (2-D) woven cloth, or three-dimensional (3-D) woven fiber preforms. The starting material is then coated with

single or multi-layered interface coatings, such as BN, to reduce strength degradation of the fibers during composite fabrication, as well as to provide a crack deflection path at or along the interface during overloading of the composite. A SiC or Si<sub>3</sub>N<sub>4</sub> layer is often deposited on these fiber coatings by CVI to protect these coatings from reacting with either molten silicon for MI-CMCs or SiC producing polymers for PIP-CMCs.

## **1.1 Limitations of the Current Technology**

The present generation SiC/SiC CMCs possess a SiC matrix which results in the CMCs possessing a relatively low proportional limit,  $\sigma_{PL}$ , due to the through-thickness cracking of the brittle matrix thereby limiting the design stresses,  $\sigma_D$ , to much less than  $\sigma_{PL}$  [5,6]. Although the SiC matrix fulfills a useful role of filling space between the SiC fiber tows in the woven fabric or preform to provide a thermally conductive path for heat transfer, these CMCs rely almost entirely on the SiC fibers to carry the load owing to the premature cracking of the matrix during loading. Thus, the high temperature usefulness of traditional non-oxide CMCs falls well below their theoretical capabilities. Fracture toughness improvement over monolithic SiC is achieved by crack bridging and crack deflection mechanisms due to the fibers [10]. Above the matrix cracking stress, these composites show poor durability because of oxygen ingress from the external surfaces through interconnected matrix cracks to the fiber/matrix interface thereby leading to the oxidation of the boron nitride interfacial coating and premature strength degradation of the reinforcing fibers [6,11]. Therefore, the brittleness of the matrix severely constraints the design of CMCs for highly stressed components, such as high-pressure turbine blades. It is noted that in practical applications, CMCs will be protected by several layers of environmental barrier coatings (EBCs) so that the useful life of traditional CMCs are greatly dependent on the life of these coatings and the matrix cracking strength.

Irrespective of the other manufacturing details, the final step of MI SiC/SiC CMCs traditionally involves infiltrating the space between the SiC fiber tows with molten silicon [12]. Although CMCs fabricated by this technique are denser than those prepared by non-MI methods, the presence of unreacted silicon in the matrix restricts their use to below 1588 K (2400 °F) due to its low creep strength and high reactivity above this temperature. Even when the CMCs are fabricated entirely by CVI, the presence of unreacted silicon in the grain boundaries of the CVI deposited SiC can react with the protective boron nitride coating on the SiC fibers. One of the objectives of NASA's Aeronautical Science's Project is to "develop high-temperature materials for turbine engines that enable a 6 percent reduction in fuel burn for commercial aircraft, compared to current SOA materials" [13]. Key among its goals is to develop CMC for use up to 1755 K (2700 °F). The presence of unreacted silicon in current generation CMCs makes this goal unattainable without the development of ceramic composites with Si-free advanced matrices with high crack resistance.

## **1.2 Objectives**

The overall objective of the proposed research under Phases I and II was to develop a new class of high temperature, lightweight, self-healing, SiC fiber-reinforced ceramic composites termed Engineered Matrix Composites (EMCs). The proposed research was focused on developing a new matrix material designed for applications up to 1755 K (2700 °F) with an ability to blunt and self-heal matrix cracks, and to match the thermal expansion of the reinforcing SiC fibers. A matrix engineered with these capabilities is expected to increase the load bearing capabilities of SiC/SiC CMCs at high temperatures. The concept is expected to advance ceramic composite technology for applications up to 1755 K (2700 °F).

## **1.3 Potential Impact on NASA and National Aeronautics Challenges**

Carbon dioxide emissions due to global air travel are currently 2 percent of total global CO<sub>2</sub> emissions [14]. Clearly, a reduction in the global emission of greenhouse gases and an increased engine

efficiency by increasing combustion temperature capabilities is of immediate importance for NASA, the United States and the global community. It is expected that a successful development of the proposed concept to TRL 9 would significantly increase engine efficiency, and considerably decrease fuel consumption and CO<sub>2</sub> greenhouse gas emissions due to air travel.

## 2.0 Theoretical Considerations in Designing Engineering Matrices

The design of engineered matrices (EMs) involves several steps:

- (a) Introduction of chemically stable and ductile second phase particles to increase the local plasticity of the matrix.
- (b) Adding constituents to self-heal cracks with low viscosity oxides or silicates.
- (c) Ensuring that the melting point of engineered matrix is higher than 1755 K (2700 °F).
- (d) Matching the thermal expansion of the engineered matrix with that of the SiC fibers to ensure compressive residual stresses in the matrix to delay or prevent crack initiation and propagation in the matrix.
- (e) Melt infiltrating with a metallic silicide instead of Si to either eliminate or minimize the presence of unreacted Si.

### 2.1 Second Phase Toughening

It is well-known that many ceramics can be toughened by ductile second phase particles, where the fracture toughness is dependent on the nonlinear deformation of the particles and their volume fraction,  $V_f$  [15]. The critical energy release rate for crack propagation,  $G_R$ , which is the work required per unit crack length to propagate the crack from  $a$  to  $a+\delta a$ , is given by

$$G_R = 2hV_f \int_0^{\epsilon_{ij}} \sigma_{ij} d\epsilon_{ij} + 2\gamma_s \quad (1)$$

where  $2h$  is the width of the process zone around the crack,  $\sigma_{ij}$  and  $\epsilon_{ij}$  are the local stresses and strains at the crack tip, and  $2\gamma_s$  is surface energy required for creating two new surfaces as the crack tip propagates to increase the length of the crack from  $a$  to  $a+\delta a$ .

Thus, if the brittle matrix in the traditional SiC/SiC CMC is suitably reformulated by adding ductile second phase particles to enhance its local plasticity at operating temperatures, then an approaching crack tip would blunt when it meets a ductile particle (Figure 1). The crack tip will be blunted if  $D \gg r$ , where  $D$  is the dimension of the ductile phase and  $r$  is the crack tip radius. Theoretical calculations reveal that the force required to propagate a blunted crack is 15 to 20 percent that to propagate a sharp crack [16]. A blunted crack is likely to stabilize and prevent the matrix from prematurely shedding the load to fibers so that the matrix cracking strength and the proportional limit of the composite should increase.

### 2.2 Engineering the Matrix for Self-Healing Cracks

A second consideration in the design of engineered matrices is to add suitable additives to the matrix to allow the formation of low viscosity oxides to flow into cracks and heal them (Figure 2). There is a considerable amount of work in the literature on additives that self-heal cracks in monolithic ceramics and CMCs [4,17,18,19,20,21,22]. In particular, carbon-carbon composites have been successfully developed with self-healing characteristics for commercial applications [4]. These studies have demonstrated that self-healing of cracks at high temperatures results in a corresponding improvement in the mechanical properties and structural life of the ceramics and ceramic composites.

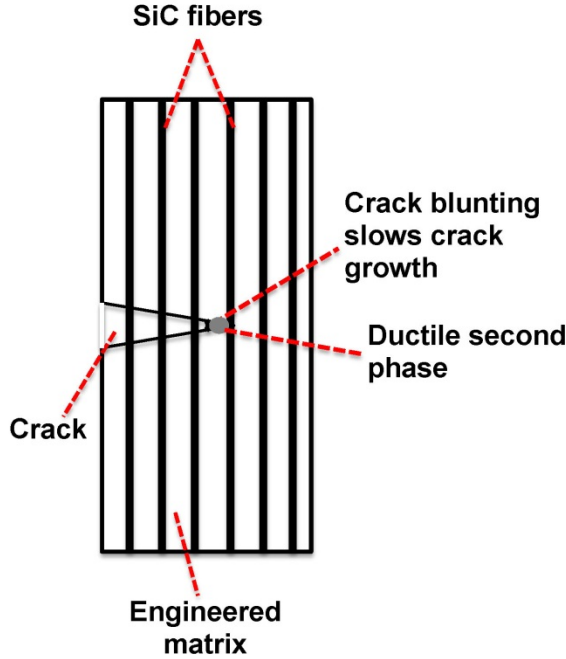


Figure 1.—Schematic showing crack tip blunting in an engineered matrix composite due to the presence of a ductile second phase.

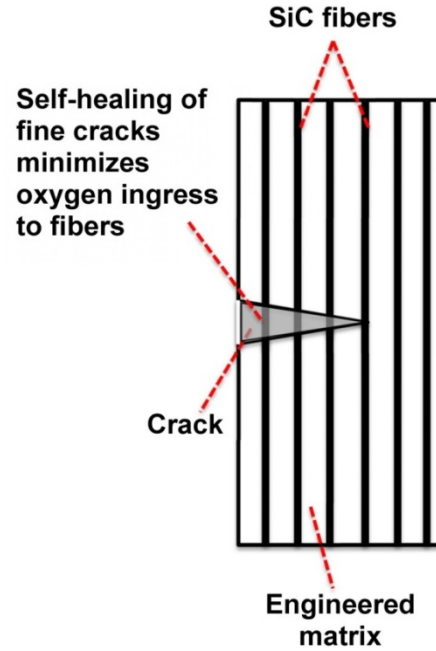


Figure 2.—Schematic showing a self-healed crack in an engineered matrix composite, which minimizes oxygen ingress.

### 2.3 Matching the Thermal Expansion of the Fibers and Matrix

Although refractory metals, such as Nb and Ta, have been used to study the ductile phase toughening of ceramics [23,24,25], these metals are unsuitable for use in SiC/SiC CMCs due to the possibility that they will react with SiC to form metallic carbides and silicides. In the present investigation, several metallic silicides were considered as potential additives to the SiC matrix to enhance the crack blunting capabilities of the matrix due to the fact that these silicides exhibit ductile-to-brittle transition temperatures (DBTT) [26]. Figure 3 compares the thermal expansions of Si [27], several silicides [28,29], SiC [28] and  $\text{Si}_3\text{N}_4$  [28]. It is evident that the thermal expansions of metallic silicides are much larger than those of SiC and deviate from it with increasing temperature. An inspection of Figure 3 demonstrates that the thermal expansion of  $\text{Si}_3\text{N}_4$  is lower than SiC thereby suggesting the possibility that a mixture of silicides and  $\text{Si}_3\text{N}_4$  could result in a matrix with a thermal expansion closer to SiC. Hebsur [30] decreased the thermal expansion of  $\text{MoSi}_2$  to match that of SCS-6 large diameter SiC fibers by adding 30 to 50 vol.%  $\text{Si}_3\text{N}_4$  to the matrix, and demonstrated that the resulting composite could be thermally cycled between 473 and 1473 K for 1000 cycles without cracking.

Similarly, an engineered matrix can be designed to theoretically match its thermal expansion to that of the fibers using a simple rule of mixtures (ROM) approach or a more sophisticated model (Figure 4). Referring to Figure 5, an engineered matrix is designed by mixing different volume fractions of three or more constituents so that the following condition is fulfilled

$$(\Delta L/L_0)_{\text{fiber}} = (\Delta L/L_0)_{\text{EM}} = V_1(\Delta L/L_0)_1 + V_2(\Delta L/L_0)_2 + V_3(\Delta L/L_0)_3 + \dots \quad (2)$$

where  $(\Delta L/L_0)_{\text{fiber}}$  is the thermal strain in the fiber,  $(\Delta L/L_0)_{\text{EM}}$  is the thermal strain in the engineered matrix,  $(\Delta L/L_0)_i$  is thermal expansion of the  $i^{\text{th}}$  constituent ( $i = 1, 2, 3, \dots, n$ ),  $V_i$  is the volume fraction of the  $i^{\text{th}}$  constituent, and  $\sum_{i=1}^n V_i = 1$ . For the specific case of an engineered matrix consisting of a silicide, SiC and  $\text{Si}_3\text{N}_4$ , Equation (2) can be expressed as

$$(\Delta L/L_0)_{\text{fiber}} = (\Delta L/L_0)_{\text{EM}} = V_{\text{silicide}}(\Delta L/L_0)_{\text{silicide}} + V_{\text{SiC}}(\Delta L/L_0)_{\text{SiC}} + V_{\text{Si}_3\text{N}_4}(\Delta L/L_0)_{\text{Si}_3\text{N}_4} \quad (3)$$

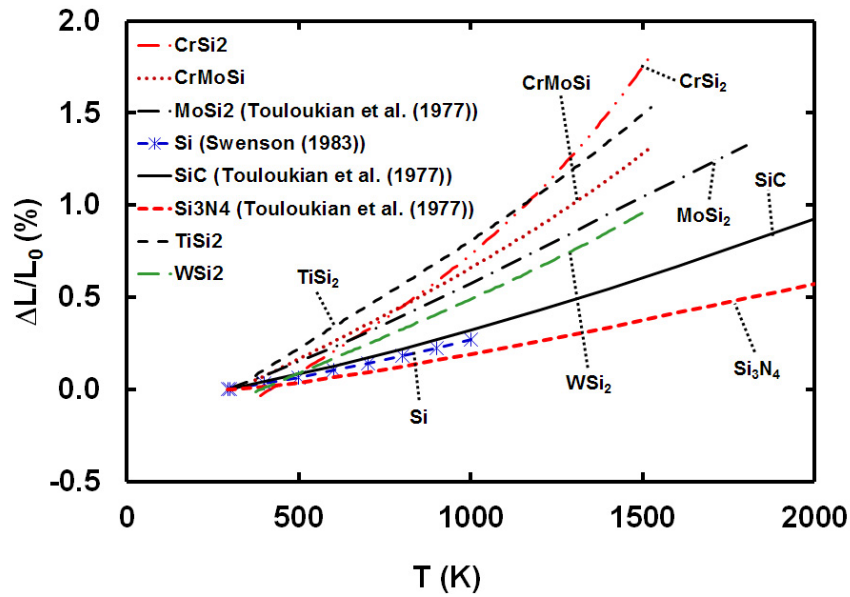


Figure 3.—Comparison of the temperature dependence of the average thermal expansion behavior of hot-pressed CrSi<sub>2</sub> [29], Cr-30%Mo-30%Si [29], MoSi<sub>2</sub> [28], Si [27], SiC [28], Si<sub>3</sub>N<sub>4</sub> [28], TiSi<sub>2</sub> [29] and WSi<sub>2</sub> [29] between 293 and 2000 K.

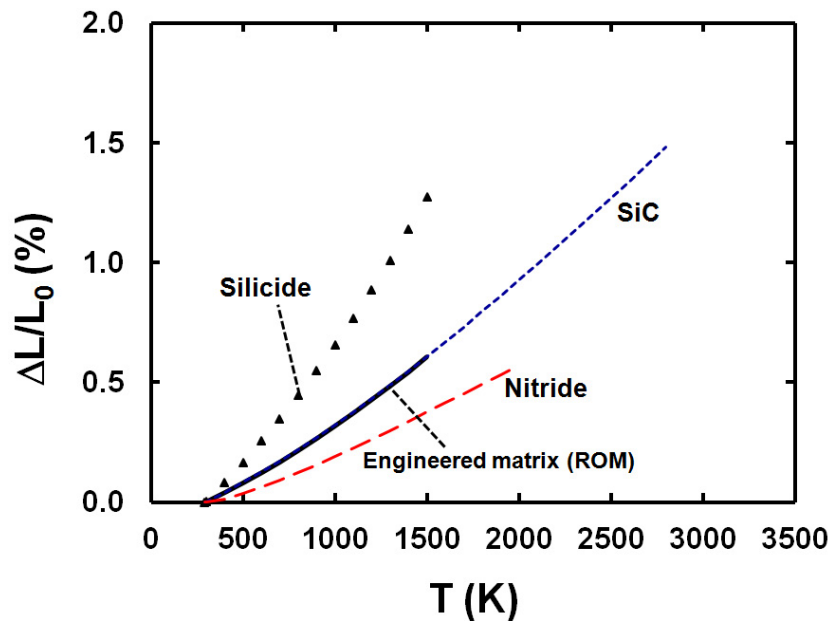


Figure 4.—Schematic showing a matrix consisting of a silicide, SiC and a nitride engineered to match its thermal expansion with that of the SiC fibers.

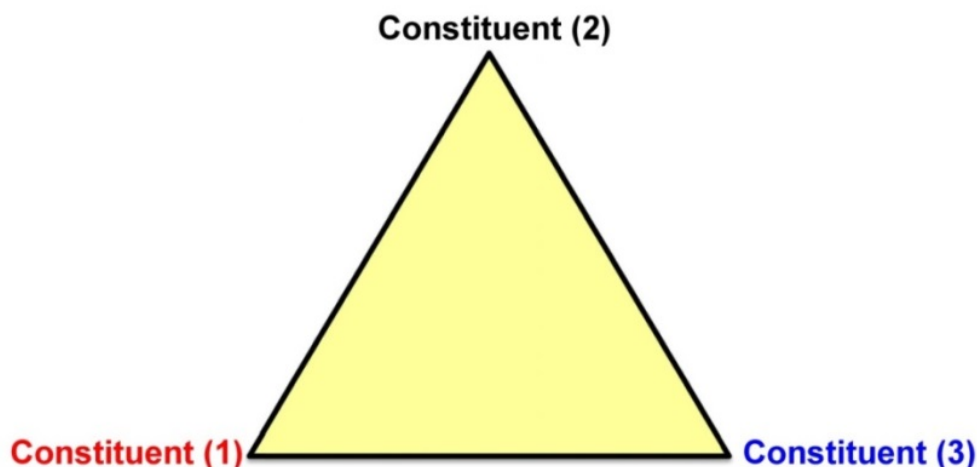


Figure 5.—Schematic showing the general concept used for designing engineered matrices with three constituents with thermal expansions matching that of SiC.

## 3.0 Experimental Procedures

### 3.1 Engineered Matrix Constituents

Commercially produced silicide powders (–325 mesh) of  $\text{CrSi}_2$ ,  $\text{TiSi}_2$ ,  $\text{WSi}_2$  and a Cr-30(at.%)Mo-30%Si (CrMoSi) alloy were used in this investigation. The CrMoSi alloy was procured from ATI Powder Metals, Pittsburgh, Pennsylvania, as gas atomized powder. Additionally, attrition milled Mo-50(vol.%)  $\text{Si}_3\text{N}_4$  from an earlier investigation [30] was used as the starting material. High purity  $\text{Si}_3\text{N}_4$  (grade SN-E10) powders were procured from Ube America, Inc., New York, New York. High purity  $\beta$ -SiC (HSC059) submicron powders were procured from the Superior Graphite Co., Chicago, Illinois.

### 3.2 Matrix Fabrication

Figure 6 shows the various processing steps used in the fabrication of engineered matrices. The major constituents, SiC,  $\text{Si}_3\text{N}_4$  and the metallic silicide were weighed in the required amount as determined using Equation (3). Unfortunately, extensive thermal expansion data as a function of temperature were not always available for some of the silicides (e.g.,  $\text{CrSi}_2$ ) used in this research so that the calculated volume fractions, and the corresponding weight fractions, for these silicides were estimated at the start of the investigation. The Mo-50(wt.%)  $\text{Si}_3\text{N}_4$  powder used in an earlier investigation [30] was reformulated by adding appropriate amounts of SiC. The powders were wet ball ground in ethanol using SiC grinding media for 48 h. After drying the powder cake, it was hand ground to powder before being hot-pressed under pure argon into the desired shape. The hot pressing temperatures varied between 1183 and 2073 K while the hot pressing stresses varied between 69 and 105 MPa for times varying between 0.25 and 4 h. Specimens were machined from the hot-pressed material for microstructural evaluation, thermal expansion measurements, oxidation studies and four-point bend testing.

### 3.3 Composite Fabrication

Attempts to fabricate EMCs using conventional slurry and melt infiltration techniques have not been completely successful. Two-dimensional fabrics woven out of Sylramic or Tyranno SA tows were used in this investigation. The Sylramic fabrics had been originally procured from Dow Corning under NASA's Enabling Propulsion Materials (EPM) program while the Tyranno SA fabrics were procured from Ube Japan under the current program. The fibers were coated with a 0.5  $\mu\text{m}$  thick layer of BN and further coated with a thicker coating of SiC by CVI at Rolls-Royce Hyper-Therm HTC, Inc., Huntington,

California. Figure 7 shows the various steps involved in the fabrication of the EMCs for infiltrating the fiber-reinforced preforms. The powders were attrition milled in ethanol using SiC or Si<sub>3</sub>N<sub>4</sub> balls for 48 h. After drying the powders, a slurry was prepared using either an Epofix cold setting resin and hardener or an aqueous solution with a pH of 9 to 10 with surfactants and water soluble epoxy binders. In the case of the epoxy resin-slurry mixture, the preforms were put in a high pressure gas chamber and evacuated with a mechanical pump before pressuring the chamber with argon gas to above 900 psi (Figure 8). In this case, the epoxy infiltrated preforms were allowed to harden overnight.

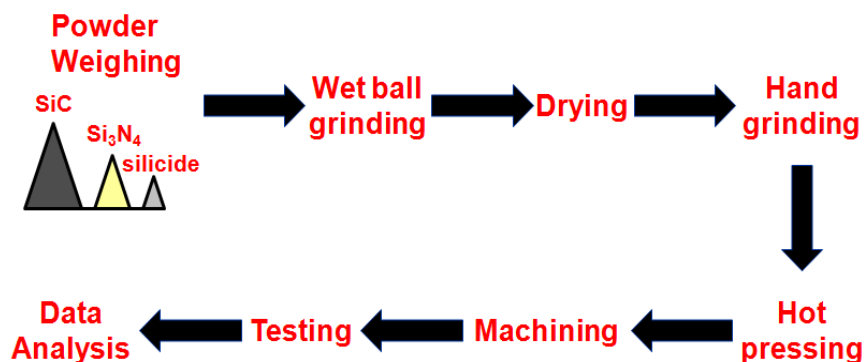


Figure 6.—Schematic showing the various processing steps used in the fabrication of the engineered matrices.

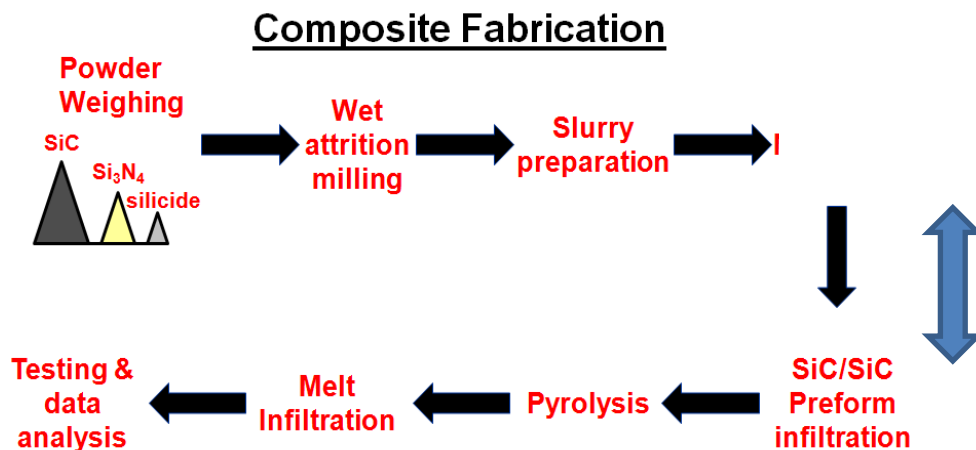


Figure 7.—Schematic showing the various processing steps used in the fabrication of the engineered matrix composites.



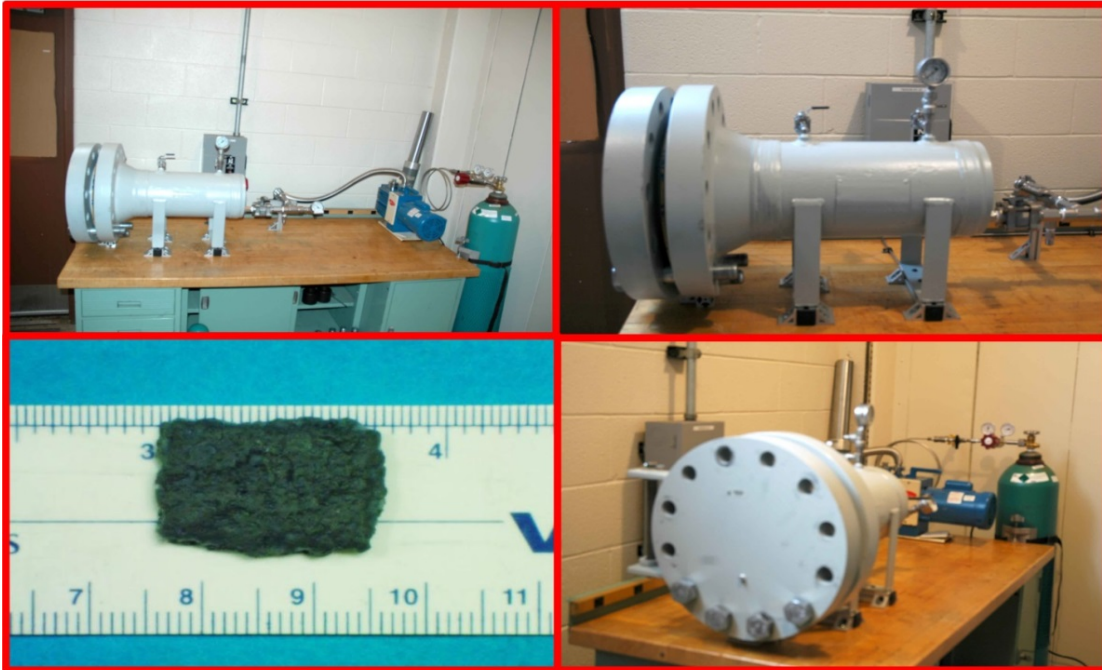


Figure 8.—Photographs of the high pressure epoxy infiltration equipment and a slurry-infiltrated SiC/SiC preform.

A second method was also attempted to infiltrate the preforms using an aqueous medium. In the absence of a dispersant, the isoelectric points (IEP), which is defined as the pH of aqueous dispersion at which the surface charge is zero, is 3.3 to 4.9 for SiC [31,32,33,34] and 6.7 for Si<sub>3</sub>N<sub>4</sub> [35], respectively. Lower values of pH result in a positive surface charge on the particles while higher pH values result in a negative surface charge. Thus, particles repel each other and remain suspended in the aqueous slurry when the pH significantly deviates from the IEP for the particles. Since IEP depends on both pH and particle size, it is important to ensure that the solution is highly acidic (i.e., low pH) or highly alkaline (high pH). Based on the results of earlier studies [31,32,33,34,35], it was preferable to prepare highly alkaline slurries with pH 9 to 10. In order to avoid contamination by alkaline ions, ammonia was used to increase the pH of the slurry.

A contract was issued to NanoSpurse, LLC, Kettering, Ohio, to develop aqueous slurry formulations. Attrition milled 20%CrSi<sub>2</sub>-55%SiC-20%Si<sub>3</sub>N<sub>4</sub>-5%CrB<sub>2</sub> and 22.5%CrMoSiGe-49%SiC-22.5%Si<sub>3</sub>N<sub>4</sub>-5%CrB<sub>2</sub> powders were first soaked overnight in a 29 (wt.%) ammonia solution. The particles were washed in water using a Buchner funnel, where the particles were filtered using a filter paper. The particles were dried in a vacuum oven maintained at 283 K under a pressure of 338.6 Pa for 2h. The slurry was prepared using 10 mL of a 10 percent Triton X100 dispersant. A 3 percent water suspended epoxy binder was added to the final formulation of the slurry, which contained 30 (wt.%) of the engineered matrix powder. Initial suspension tests revealed that the particles remained in suspension for at least 24 h. However, preforms infiltrated with these slurries under a mechanical pump vacuum did not show sufficient solids loading after one infiltration attempt. Attempts to increase the volume fractions of the particles by both particulate infiltration techniques are continuing.

The specimens were then pyrolyzed to convert the organic material to carbon before melt infiltrating with either Si or Si-1(at.%)Ge alloy. Melt infiltration was conducted in a chamber evacuated to a vacuum level of about  $1.3 \times 10^{-4}$  Pa ( $\sim 1 \times 10^{-6}$  torr). Alternate to the traditional melt infiltration with Si, attempts were made to infiltrate the preforms with CrSi<sub>2</sub> or Cr-25(wt.%)Si. Here too, more work is needed to completely infiltrate the preforms.



### **3.4 Materials Characterization**

#### **3.4.1 Microstructural and Non-Destructive Characterization**

Specimens were cut, mounted and polished for metallographic examination by optical and scanning electron microscopy (SEM). Computerized tomography (CT) scans were used to determine the extent of particle and melt infiltration of the preforms, and these images were compared with the microstructural results.

#### **3.4.2 Thermal Expansion Measurements**

Thermal expansion measurements were conducted on hot-pressed cylindrical specimens 25.4-mm long and 9.5-mm in diameter using a NETZSCH Dilatometer Model DIL 402C equipped with a high purity alumina as a calibration standard, where the two faces were machined to ensure that they were flat and parallel. Measurements were made over three heat-cool cycles to (a) minimize the effects of compositional, microstructural and processing variables on the data, (b) determine the extent of scatter in the data, and (c) to evaluate statistical averages of the coefficients for the regression curve. The specimen was placed in a sample holder and aligned with a single push-rod under an applied constant load of 0.2 N. The specimens were heated from 293 to 1523 K at 10 K/min. in the first cycle and cooled to 373 K at 10 K/min. in the first cool-down cycle. Subsequent cycles consisted of heating and cooling between 373 and 1523 K. All measurements were conducted in a He atmosphere flowing at 60 cc/min. The length changes were recorded by a computerized data acquisition system. The experimental strain,  $\Delta L/L_0$ , where  $\Delta L$  is the differential change in length,  $L-L_0$ , and  $L_0$  is the original length of the specimen at room temperature, were measured.

#### **3.4.3 Isothermal Oxidation**

The engineered matrices that were formulated with different metallic silicide constituents were isothermally oxidized at 1600 K for 100 h. The nominal dimensions of the oxidation specimens were 13.5 mm in diameter and 3 mm thick. Each specimen had a 2.5 mm diameter hole machined by electro-discharge machining (EDM) about 3.2 mm from the edge to allow it to hang from a quartz hook in a thermogravimetric analyzer (TGA) equipped with a weighing balance to periodically monitor the weight. The data were logged by a computer data acquisition system. Oxidation was conducted in dry air flowing at 100 sccm.

#### **3.4.4 Mechanical Testing**

Four-point bend tests were conducted on engineered matrices where the nominal specimen dimensions were 50 x 4 x 3-mm. These specimens were machined flat and parallel from hot-pressed plates 50 x 50 x 3-mm in dimensions using a diamond saw. Bend tests were conducted in air between room temperature and 1698 K in a servo-hydraulic uniaxial testing machine at a speed of  $8.3 \times 10^{-3}$  mm/s corresponding to an approximate engineering strain rate of  $2 \times 10^{-3}$  s<sup>-1</sup>.

#### **3.4.5 Self-Healing Studies**

Several CrSi<sub>2</sub>/SiC and CrMoSi/SiC matrices were formulated without Si<sub>3</sub>N<sub>4</sub> to study the effect of CrB<sub>2</sub>, Ge, Y and ZrSiO<sub>4</sub> additives on self-healing cracks and holes. These compositions were prepared as described in Section 3.2 and hot-pressed into disks 12.7 mm diameter and 3.2 mm thickness. Initial attempts to indent these specimens with a Vickers hardness indent to generate cracks were unsuccessful. Instead, a 1 mm diameter hole was drilled in each specimen before annealing them in air in a rapid heating box furnace. The specimens were oxidized either at 1600 or 1700 K for a cumulative oxidation time of 100 h, and the oxidized specimens were microstructurally examined to study the extent of scratch healing and hole closure. Other tests that are underway involve studying the effects of the additives on healing cracks developed from hardness indents (Figure 9).



Figure 9.—Photograph of a Vickers hardness indent showing cracks (red arrows) emanating from it. These specimens will be oxidized at high temperatures to study the effect of additives on the self-healing of these cracks.

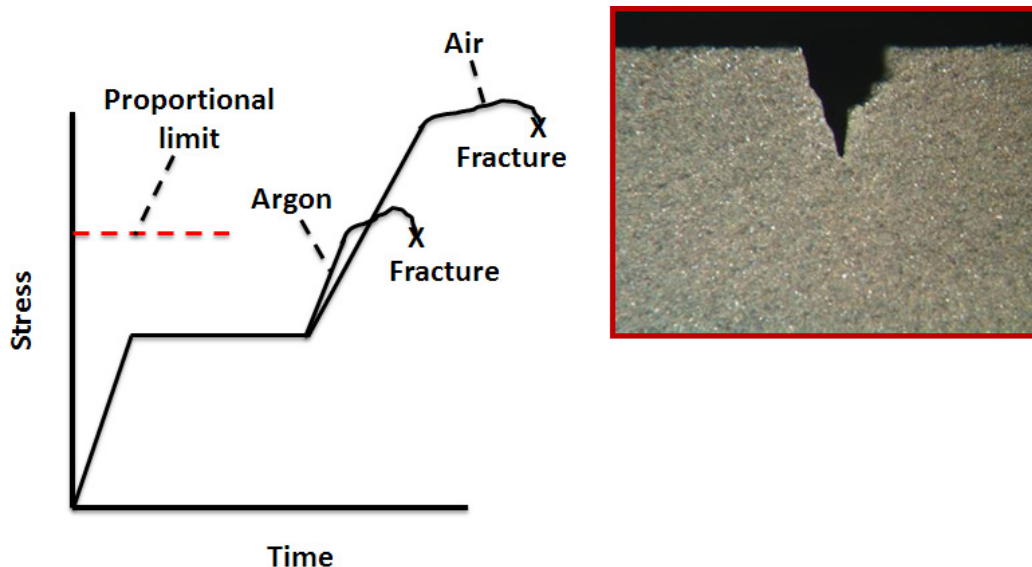


Figure 10.—Photograph of a bend specimen showing a SEPB notch. The notched specimens will be tested in air and inert gas to demonstrate that the air-tested specimens are stronger than those tested in inert gas due to self-healing of cracks as shown in the schematic figure on the left.

Based on these observations, several  $\text{CrSi}_2/\text{SiC}/\text{Si}_3\text{N}_4$  and  $\text{CrMoSi}/\text{SiC}/\text{Si}_3\text{N}_4$  engineered matrices were formulated and hot-pressed into 50 x 50 x 3 mm plates. Several bend specimens with dimensions 50 x 4 x 3-mm were machined for fracture toughness testing in argon and air using the single edge V-notched beam (SEVNB) method [36]. These tests are still underway and only preliminary results are reported in this report. Sharp notches were cut into the specimens to help initiate cracks during loading (Figure 10). These specimens will be tested in air and argon to demonstrate the self-healing of the notch as shown in the schematic stress-strain curve. Elastic moduli,  $E_{\text{MOD}}$ , measurements were conducted on some specimens before and after heat treatment in air and argon at 1700 K using the Impulse Excitation

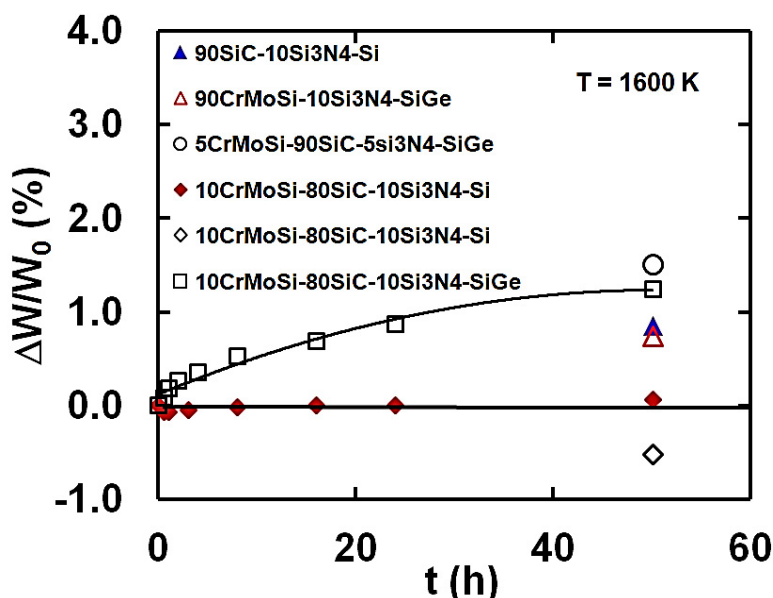


Figure 11.—Relative weight change versus oxidation time for slurry and melt-infiltrated SiC/SiC preforms.

technique [37,38,39]. The desired loading profile shown in Figure 10 could not be precisely followed since the elastic moduli measurements indicated that the specimens were porous. Thus, the SEVNB specimens were pre-annealed at 1698 K for 1800 s prior to loading.

Four-point bend tests were conducted on the slurry infiltrated and melt infiltrated composite specimens at room temperature and 1645 K. Tests were also conducted on uninfiltrated preforms. In order to study the effect of self-healing without additives, some infiltrated composite specimens were pre-cracked at room temperature on a three-point bend fixture, heat-treated at 1600 K for 50 h and re-tested at 1645 K. The self-healing times were determined by oxidizing small specimens at 1600 K for different lengths of time and measuring the relative weight change as a function of oxidation time (Figure 11). As shown in Figure 11, the curves flatten out at about 50 h.

## 4.0 Results and Discussion

### 4.1 Thermal Expansion and Proof-of-Concept

#### 4.1.1 Microstructures of Thermal Expansion Specimens

Microstructural observations of the hot-pressed matrix specimens revealed that most of them were well-consolidated although the extent of homogeneity varied from one composition to another. Figure 12(a) shows a photograph of a hot-pressed 10(wt.%)CrMoSi-60%SiC-30%Si<sub>3</sub>N<sub>4</sub> (CrMoSi-EM) specimen while Figure 12(b) and (c) show the corresponding optical, and back-scattered electron microscopy (BSE) images and energy dispersion spectra (EDS), respectively, where it was observed that the white particles were CrMoSi. The microstructure was fairly homogenous. Figure 13(a) to (c) show the optical micrographs of 10(wt.%)CrSi<sub>2</sub>-70%SiC-20%Si<sub>3</sub>N<sub>4</sub> (CrSi<sub>2</sub>-EM), 10(wt.%)TiSi<sub>2</sub>-70%SiC-20%Si<sub>3</sub>N<sub>4</sub> (TiSi<sub>2</sub>-EM) and 10(wt.%)WSi<sub>2</sub>-70%SiC-20%Si<sub>3</sub>N<sub>4</sub> (WSi<sub>2</sub>-EM), respectively, where the degree of homogeneity varied between the three engineered matrices. These microstructures did not contain any significant amount of cavities. Figure 14 shows the BSE image for a TiSi<sub>2</sub>-EM specimen, where the EDS show that the gray particles are Ti-poor (Region C) while the white particles are TiSi<sub>2</sub> (Region D). The WSi<sub>2</sub>-EM specimen unexpectedly had several white W-rich (Region A) and gray Si-rich (Region B) particles (Figure 15 and Figure 16). The source of the tungsten particles was attributed to the WSi<sub>2</sub> powder used in fabricating these matrices.

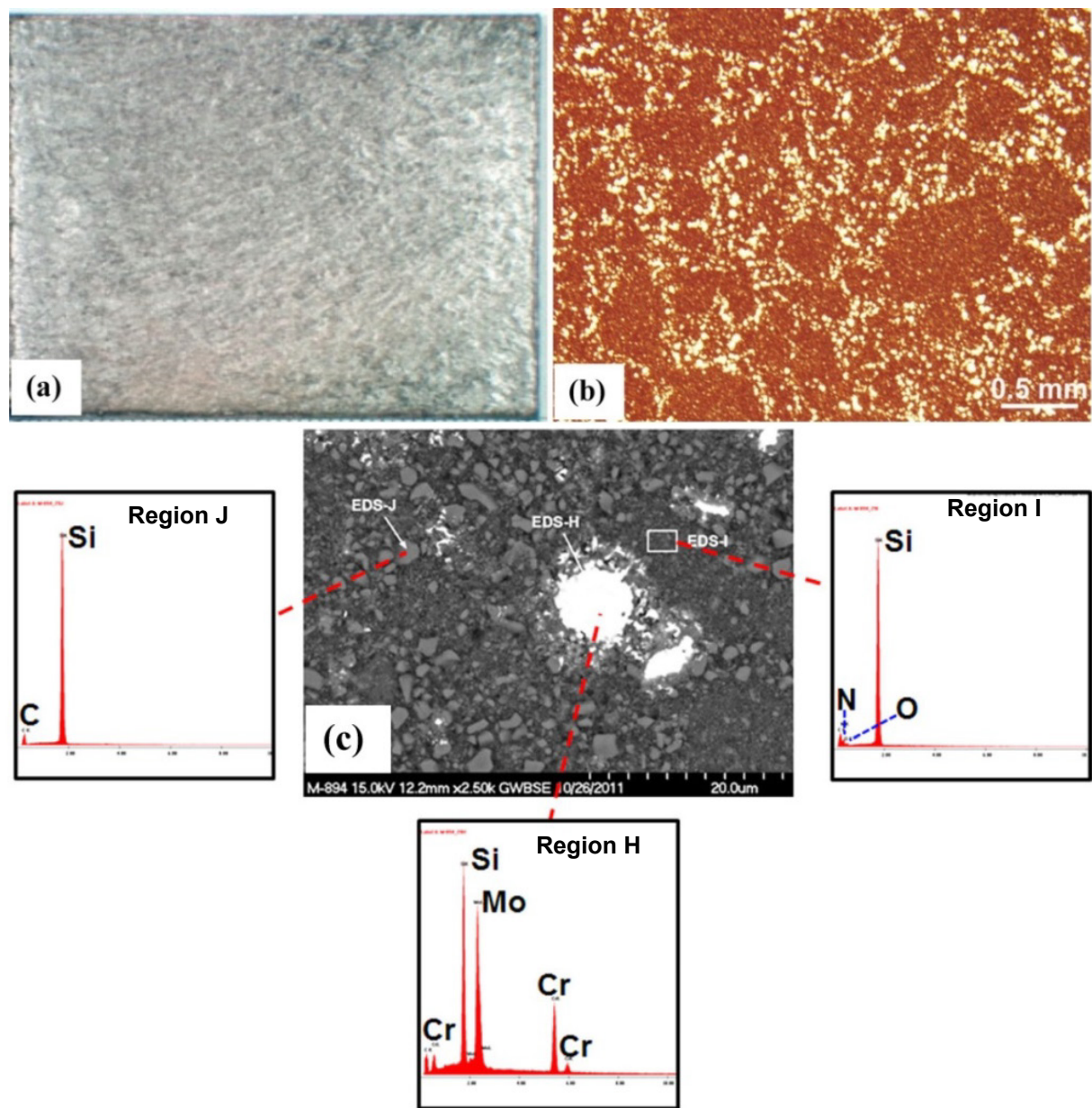


Figure 12.—(a) Photograph of hot-pressed 10(wt.%)CrMoSi-60%SiC-30%Si<sub>3</sub>N<sub>4</sub> engineered matrix; (b) optical micrograph; and (c) back-scattered electron micrograph and energy dispersion spectra.



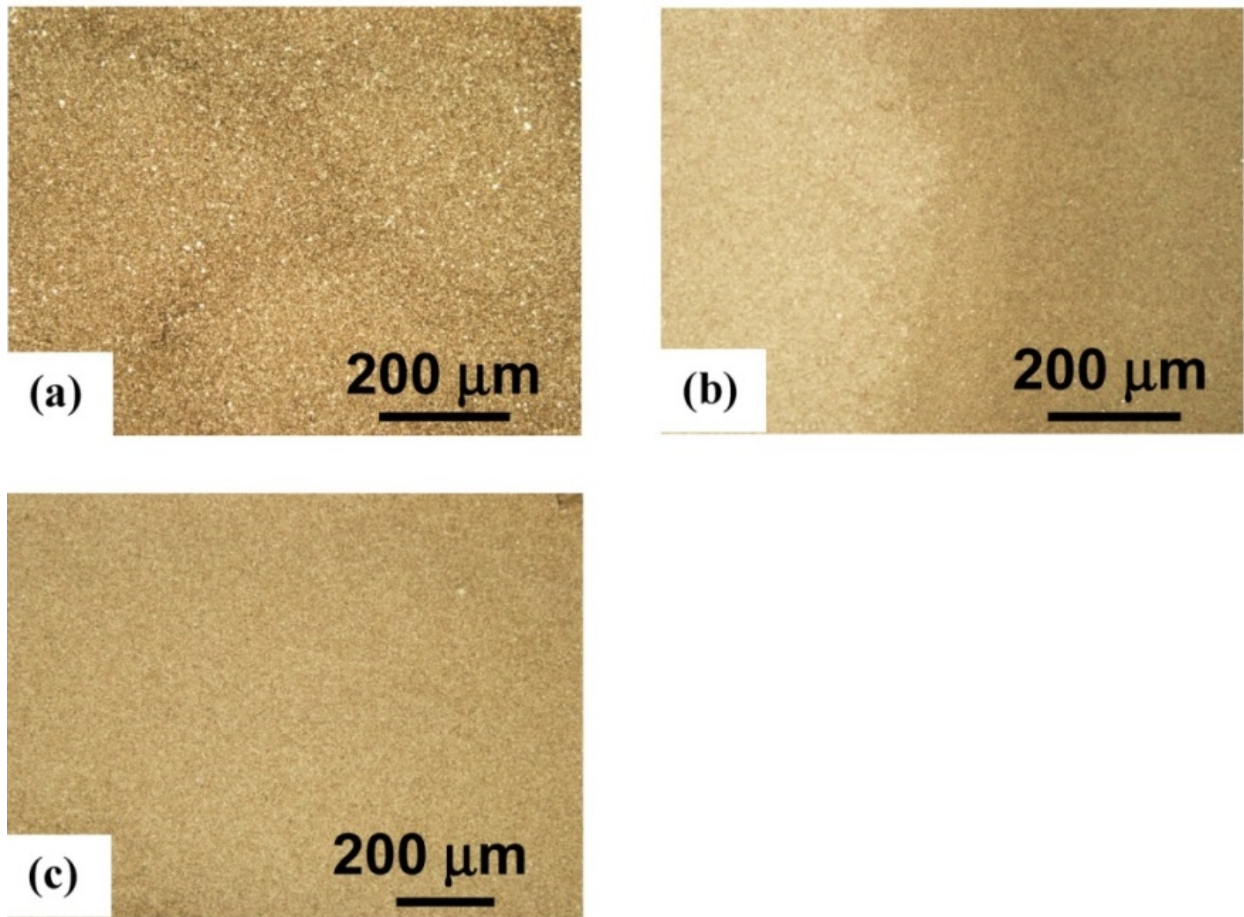


Figure 13.—Optical micrographs of hot-pressed engineered matrices: (a) 10(wt.%)CrSi<sub>2</sub>-70%SiC-20%Si<sub>3</sub>N<sub>4</sub>; (b) 10(wt.%)TiSi<sub>2</sub>-70%SiC-20%Si<sub>3</sub>N<sub>4</sub>; and (c) 10(wt.%)WSi<sub>2</sub>-70%SiC-20%Si<sub>3</sub>N<sub>4</sub>.

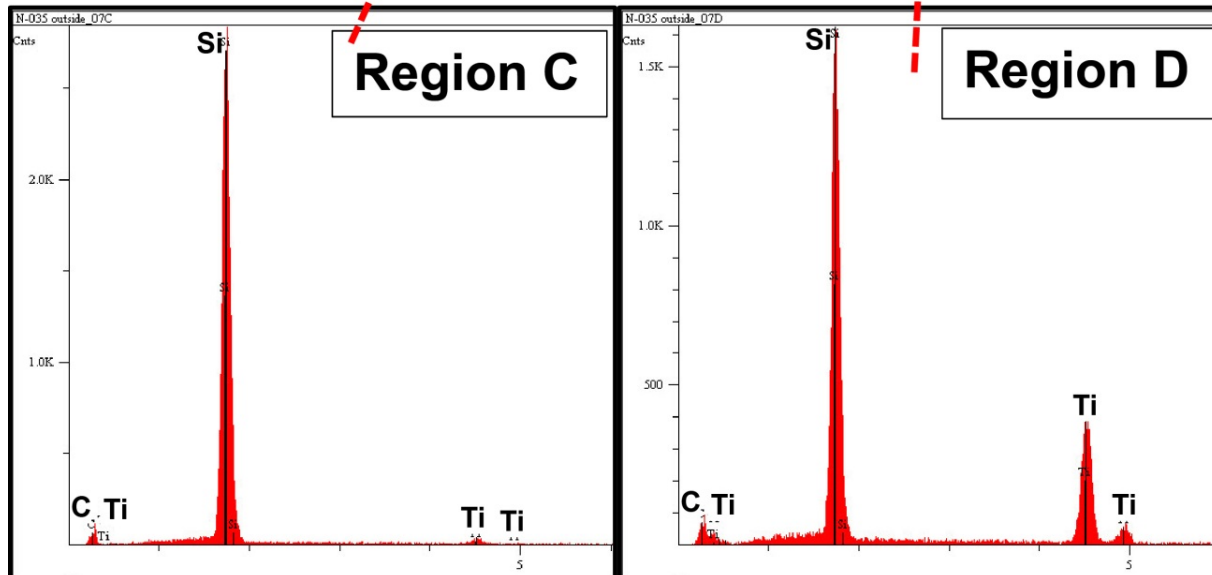
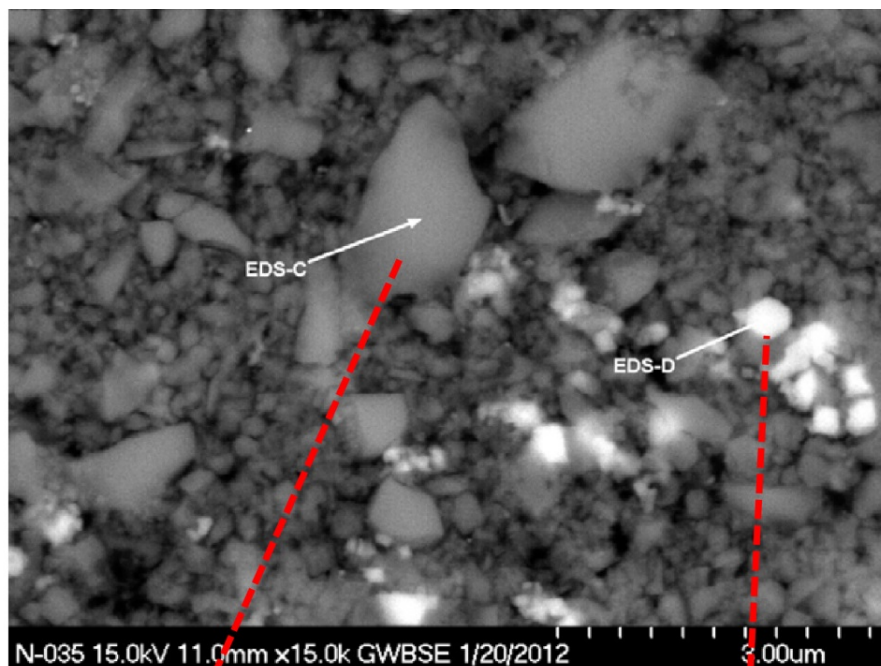


Figure 14.—Back-scattered image of hot-pressed 10(wt.%)TiSi<sub>2</sub>-70%SiC-20%Si<sub>3</sub>N<sub>4</sub> engineered matrix and energy dispersion spectra of regions C and D showing gray Si-rich and white TiSi<sub>2</sub> particles, respectively.

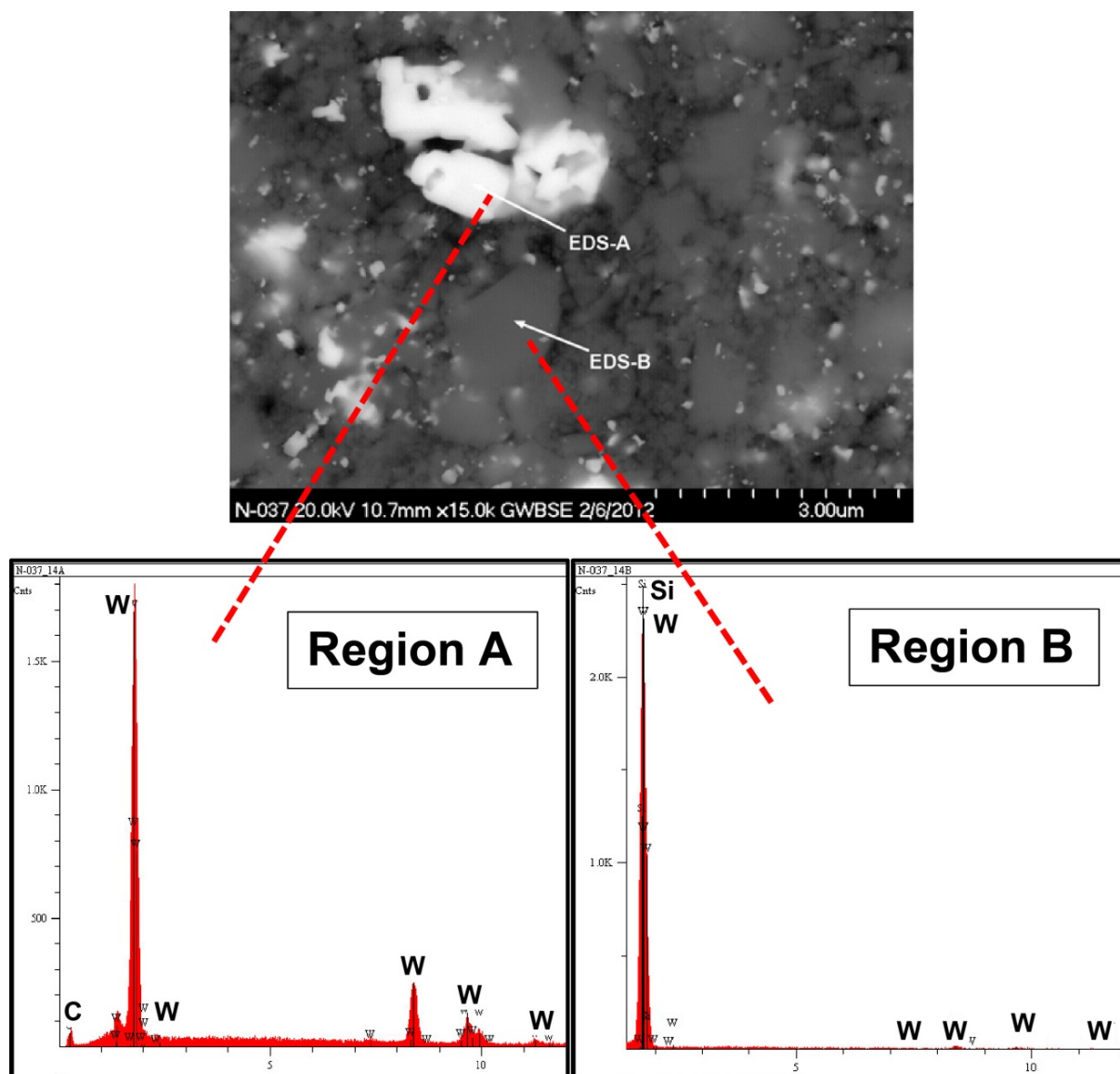


Figure 15.—Back-scattered image of hot-pressed 10(wt.%)WSi<sub>2</sub>-70%SiC-20%Si<sub>3</sub>N<sub>4</sub> engineered matrix and energy dispersion spectra of regions A and B showing W and WSi<sub>2</sub> particles, respectively.

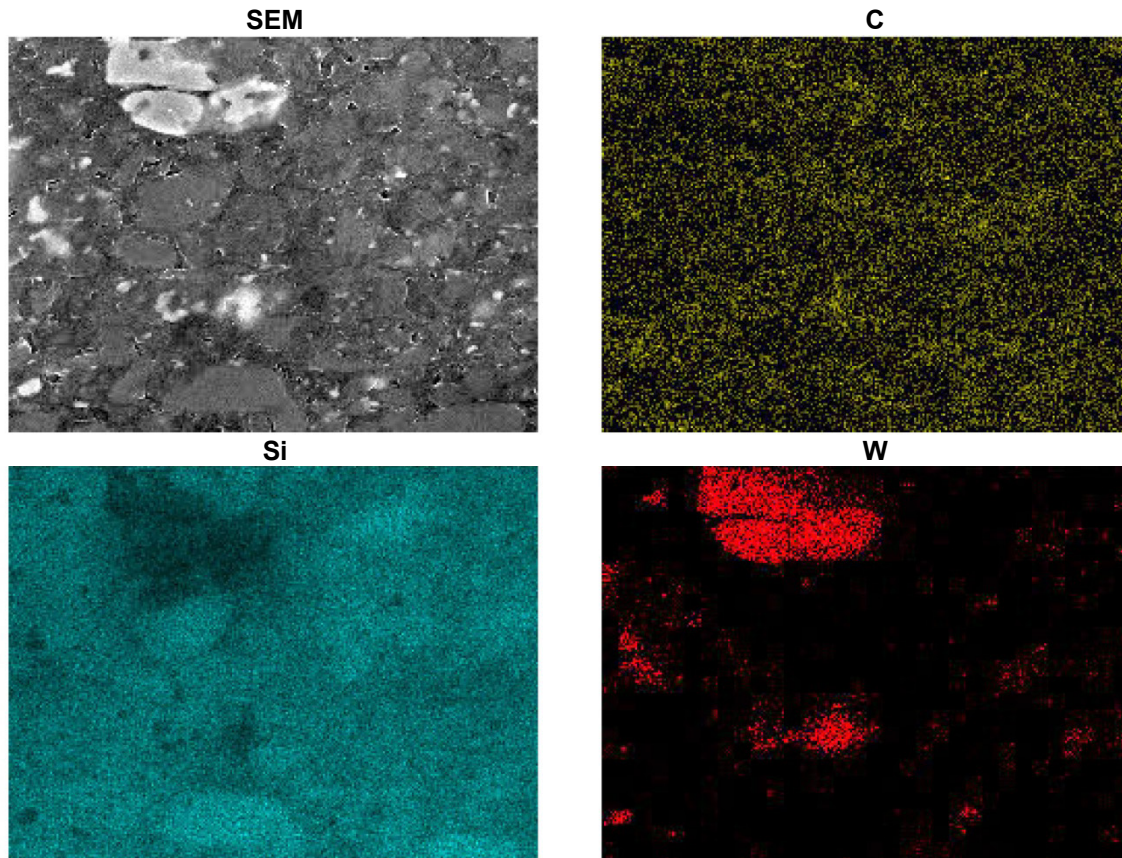


Figure 16.—Scanning electron image of hot-pressed 10(wt.%) $\text{W}\text{Si}_2$ -70% $\text{SiC}$ -20% $\text{Si}_3\text{N}_4$  engineered matrix and C, Si and W x-ray maps showing W and  $\text{W}\text{Si}_2$  particles, respectively.

#### 4.1.2 Thermal Expansion of Silicides

Details of the thermal expansion data generated on the disilicides and the  $\text{CrMoSi}$  alloy in this investigation are reported in detail elsewhere [29]. For some silicides, the thermal expansion during the first heat-up cycle was different than those in the subsequent cool-down and heat-up cycles. This difference in behavior was attributed to the effect of residual stresses generated during cool down from the hot-pressing temperatures, which are annealed out after the first heat-up cycle [40]. Figure 17(a) shows an example of the thermal expansion data for the three heat-cool cycles for  $\text{CrSi}_2$ . Neglecting the data from the first heat-up cycle, the data from the first cool-down to the third cool-down cycles were fitted with equation (4):

$$(\Delta L/L_0)_{\text{thermal}} = A(T-293)^3 + B(T-293)^2 + C(T-293) + D \quad (4)$$

where,  $(\Delta L/L_0)_{\text{thermal}}$  is the magnitude of the  $\Delta L/L_0$  without any residual processing strains,  $T$  is the absolute temperature,  $A$ ,  $B$ ,  $C$  and  $D$  are regression constants. Table I compiles the values of the regression constants and the corresponding coefficients of determination,  $R_d^2$ , for the  $\text{CrSi}_2$  specimens from three hot-press runs.<sup>1</sup> Figure 17(b) compares the regression plots for the three specimens, where it is seen that the curves are reasonably close thereby suggesting that batch-to-batch variability is relatively small. Unfortunately, a sparsity of published data on polycrystalline  $\text{CrSi}_2$  did not permit a meaningful comparison with the present results.

<sup>1</sup> The specimen from Run 582 had more porosity than those from Runs 619 and 620.



TABLE I.—VALUES OF THE REGRESSION CONSTANTS  
FOR  $\text{CrSi}_2$  SPECIMENS FROM THREE HOT-PRESS RUNS

Hot press run no.	$A,$ $\text{K}^{-3}$	$B,$ $\text{K}^{-2}$	$C,$ $\text{K}$	$D,$ $\%$	$R_d^2$
582	$2.0 \times 10^{-10}$	$1.2 \times 10^{-7}$	$1.0 \times 10^{-3}$	$-1.8 \times 10^{-1}$	0.993
619	$4.2 \times 10^{-10}$	$-1.4 \times 10^{-7}$	$1.1 \times 10^{-3}$	$-1.4 \times 10^{-1}$	0.999
620	$4.2 \times 10^{-10}$	$-1.8 \times 10^{-7}$	$1.1 \times 10^{-3}$	$-9.3 \times 10^{-2}$	0.999

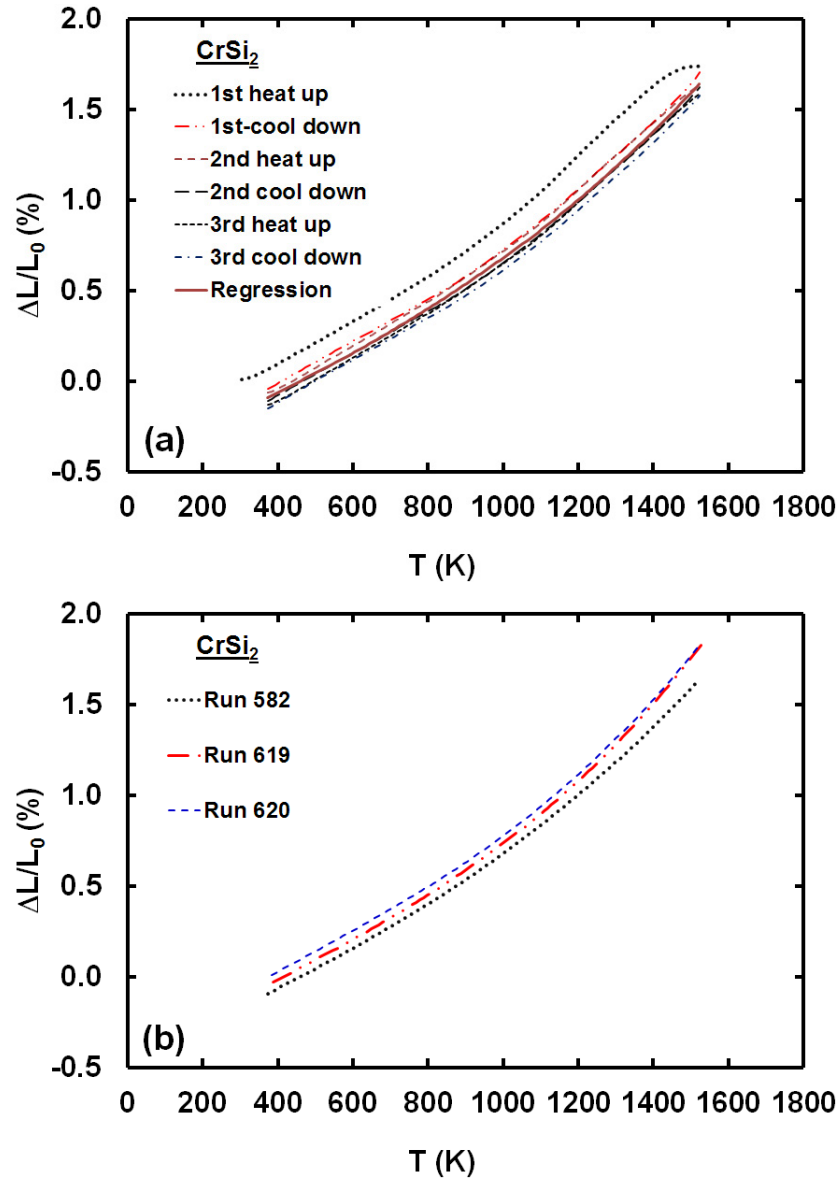


Figure 17.—Temperature dependence of the thermal expansion behavior of (a) a  $\text{CrSi}_2$  specimen during three heat up-cool down cycles between 293 and 1523 K; and (b) comparison of the regression equations for three  $\text{CrSi}_2$  specimens between 303 and 1523 K.

Figure 18(a) to (c) show the thermal expansion behaviors of the CrMoSi, TiSi<sub>2</sub> and WSi<sub>2</sub>, respectively, for three heat-cool cycles. There was no significant difference in the thermal expansion behavior for the CrMoSi and TiSi<sub>2</sub> between the first heat-up and the other thermal cycles. In contrast, the WSi<sub>2</sub> exhibits somewhat higher values of  $\Delta L/L_0$  in the first heat-up cycle than in the subsequent cycles although the difference was not as large as for the CrSi<sub>2</sub> specimens. Table II gives the values of the regression constants and  $R_d^2$  for these three silicides. Since the CrMoSi alloy was prepared by replacing Cr with Mo in Cr<sub>3</sub>Si [41], it is reasonable to compare its thermal expansion with that for Cr<sub>3</sub>Si [28]. The addition of Mo appears to decrease the thermal expansion of Cr<sub>3</sub>Si slightly at the higher temperatures. The present values of  $\Delta L/L_0$  are in reasonable agreement with the literature values for TiSi<sub>2</sub> and WSi<sub>2</sub> although the deviation in the two sets of data slightly increases with increasing temperature [28].

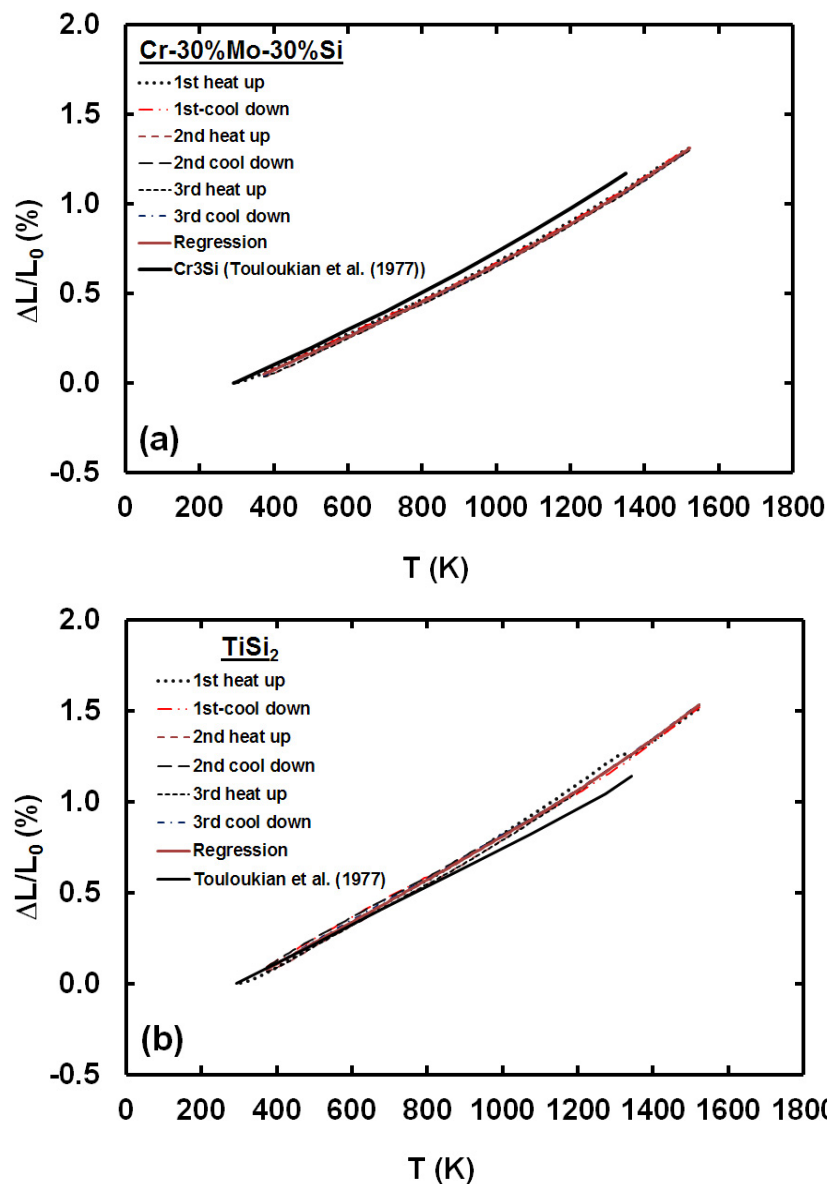


Figure 18.—Continued.

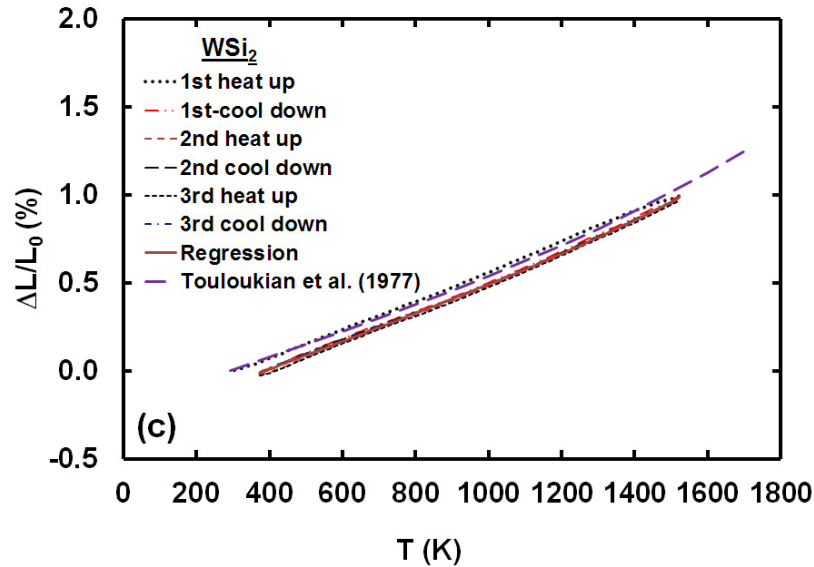


Figure 18.—Concluded. Temperature dependence of the thermal expansion behaviors of (a) a Cr-30(at.%)Mo-30%Si specimen, (b)  $\text{TiSi}_2$  and (c)  $\text{WSi}_2$  during three heat up-cool down cycles between 293 and 1523 K. The literature data for  $\text{Cr}_3\text{Si}$ ,  $\text{TiSi}_2$  and  $\text{WSi}_2$  are also shown in the figure for comparison [28].

TABLE II.—VALUES OF THE REGRESSION CONSTANTS AND COEFFICIENTS OF DETERMINATION FOR Cr-30%Mo-30%Si,  $\text{TiSi}_2$  AND  $\text{WSi}_2$

Alloy	$A, \text{K}^{-3}$	$B, \text{K}^{-2}$	$C, \text{K}$	$D, \%$	$R_d^2$
CrMoSi	$1.3 \times 10^{-10}$	$-1.7 \times 10^{-8}$	$9.2 \times 10^{-4}$	$-2.5 \times 10^{-2}$	0.9993
$\text{TiSi}_2$	$1.8 \times 10^{-10}$	$-1.7 \times 10^{-7}$	$1.2 \times 10^{-3}$	$-2.0 \times 10^{-2}$	0.999
$\text{WSi}_2$	$1.2 \times 10^{-10}$	$-1.2 \times 10^{-7}$	$8.3 \times 10^{-4}$	$-8.0 \times 10^{-2}$	0.999

#### 4.1.3 Effect of $\text{Si}_3\text{N}_4$ Addition on Thermal Expansion

As demonstrated in Figure 3, the magnitudes of  $\Delta L/L_0$  for silicides are larger than that for SiC and  $\text{Si}_3\text{N}_4$  with the extent of deviation increasing with increasing temperature. In order to minimize this difference in  $\Delta L/L_0$ , it was proposed that the addition of 50(vol.%) of  $\text{Si}_3\text{N}_4$  to  $\text{MoSi}_2$  can decrease its thermal expansion to values close to those of SiC [30]. However, a close examination of the heat-cool cycles for this material suggested that its thermal expansion behavior was somewhat more complex due to the development of residual stresses during thermal cycling [42] (Figure 19). Similarly, the thermal expansion of a  $\text{TiSi}_2$ -80(vol.%)  $\text{Si}_3\text{N}_4$  material is close to that of SiC [28] only during the first heat-up cycle (Figure 20). However, its thermal expansion deviated from that of SiC during subsequent cool-down and heat-up cycles due to the development of thermal residual stresses in the matrix.

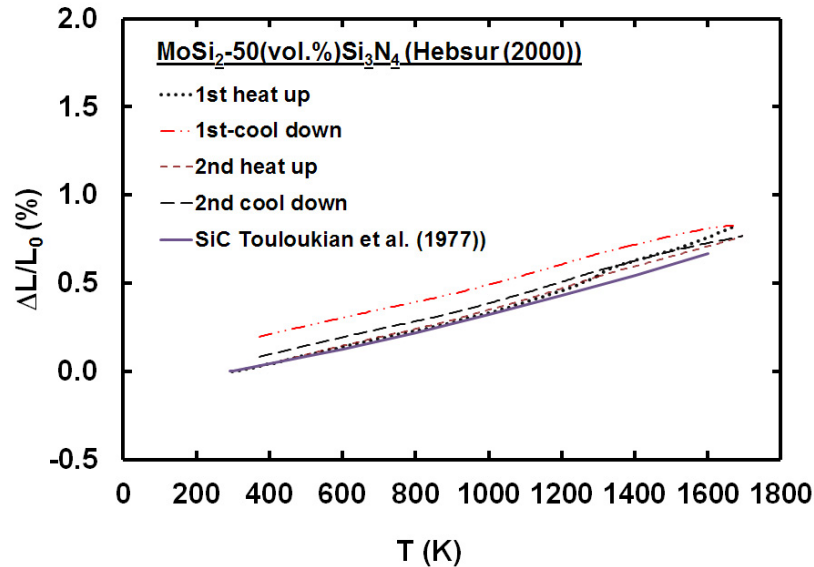


Figure 19.—Temperature dependence of the thermal expansion behavior of a  $\text{MoSi}_2\text{-50(vol.}\%\text{Si}_3\text{N}_4$  specimen during three heat up-cool down cycles between 293 and 1688 K [42]. The data for SiC is included for comparison [28].

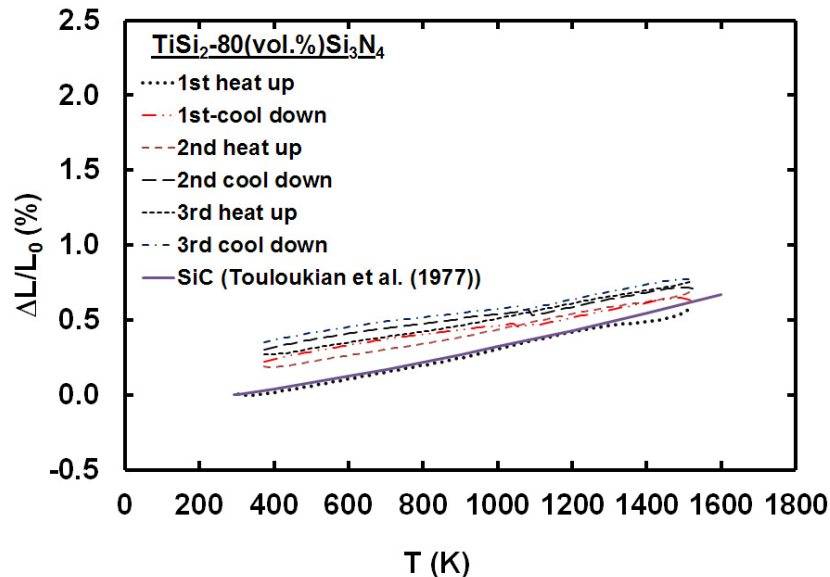


Figure 20.—Temperature dependence of the thermal expansion behavior of  $\text{TiSi}_2\text{-80(vol.}\%\text{Si}_3\text{N}_4$  during three heat up-cool down cycles between 293 and 1523 K. The literature data for SiC is also shown in the figure for comparison [28].

#### 4.1.4 Thermal Expansion Data for Engineered Matrices

As noted above, the design of an engineered matrix cannot simply involve mixing a silicide and  $\text{Si}_3\text{N}_4$  in appropriate amounts in order to match the thermal expansion with that of the SiC fibers. The resulting magnitudes of the thermal stresses can eventually become significant after several cycles and result in the catastrophic failure of the matrix. However, formulating the matrix in accordance with Equation (3) as described in Section 2.3 generally results in a thermally stable matrix capable of withstanding several thermal cycles (Figure 21(a) to (e)). Figure 21(a) demonstrates the almost close correspondence of the  $\Delta L/L_0$  values for  $\text{CrSi}_2\text{-EM}$  and SiC [28] between 293 and 1523 K during both the

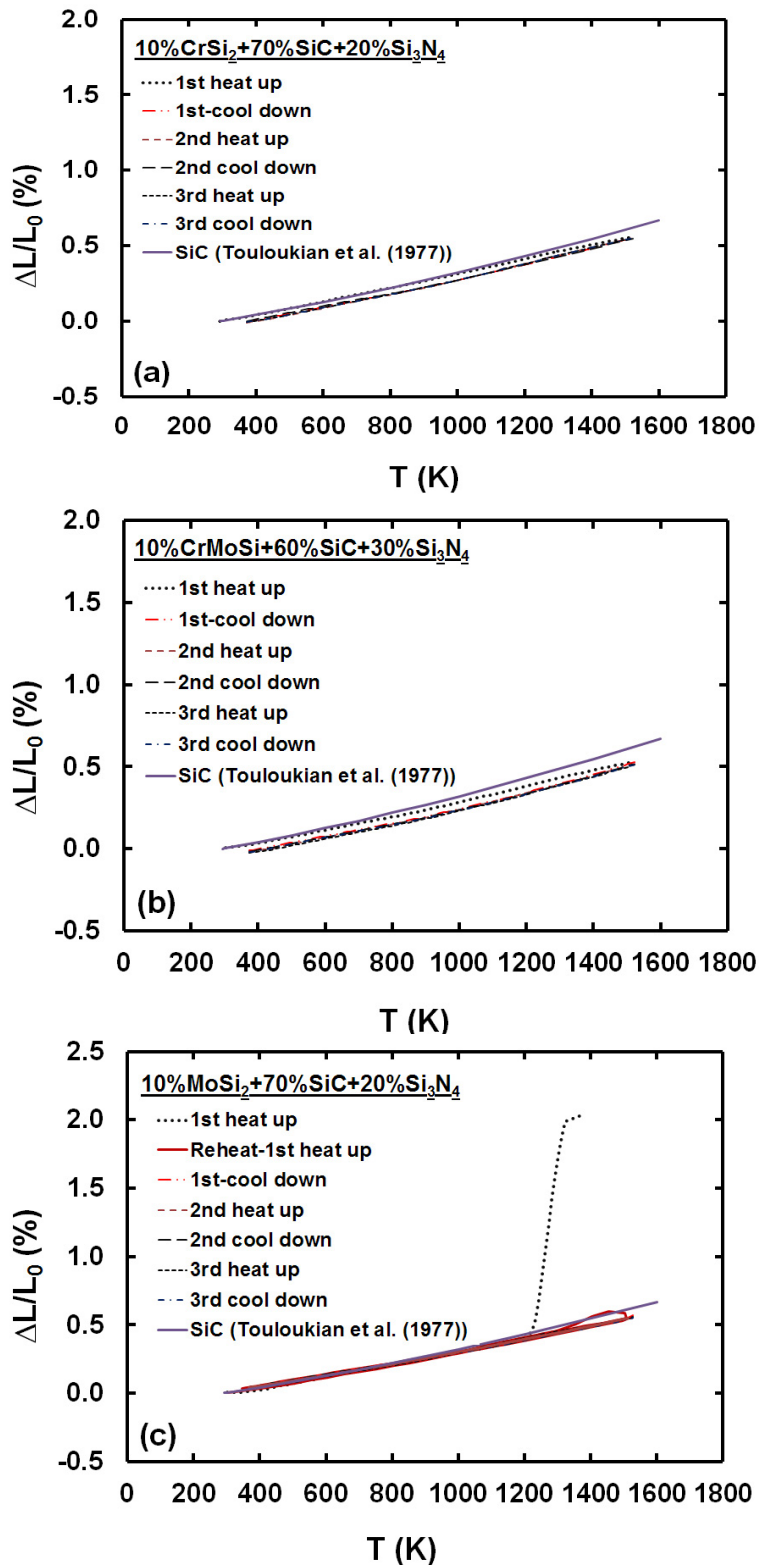


Figure 21.—Continued.

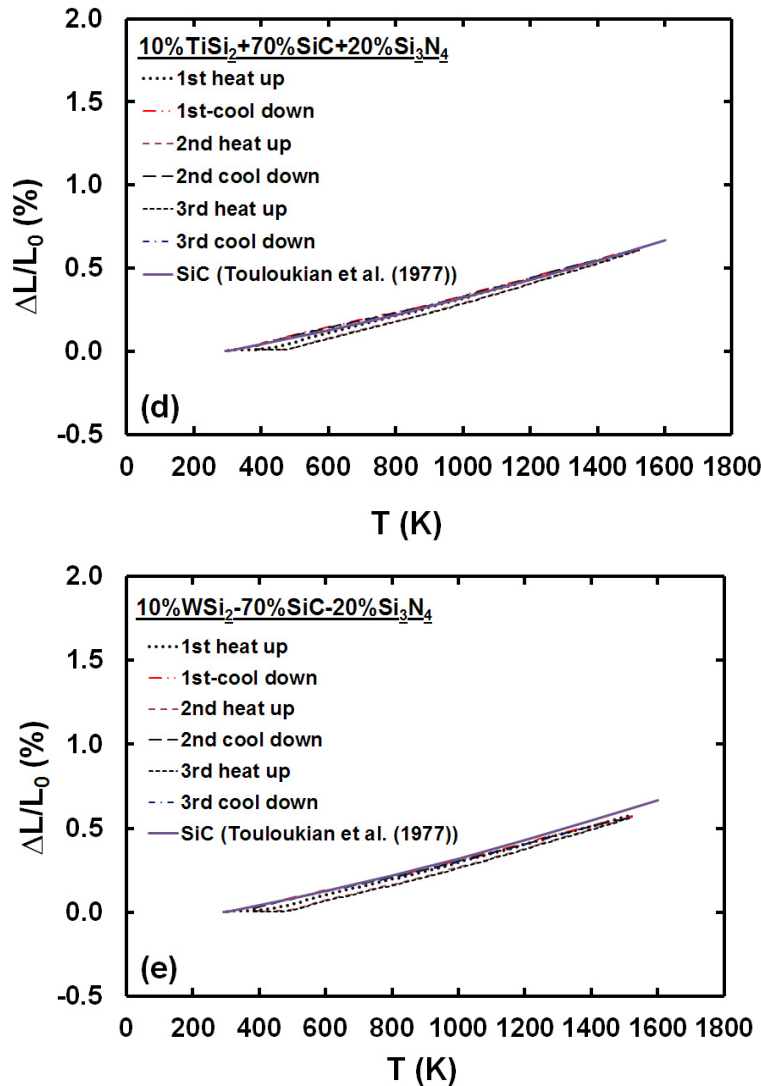


Figure 21.—Concluded. Temperature dependence of the thermal expansion behaviors of (a) 10%CrSi<sub>2</sub>-70%SiC-20%Si<sub>3</sub>N<sub>4</sub>; (b) 10%CrMoSi-60%SiC-30% Si<sub>3</sub>N<sub>4</sub>; (c) 10%MoSi<sub>2</sub>-70%SiC-20%Si<sub>3</sub>N<sub>4</sub>; (d) 10%TiSi<sub>2</sub>-70%SiC-20%Si<sub>3</sub>N<sub>4</sub>; and (e) 10%WSi<sub>2</sub>-70%SiC-20%Si<sub>3</sub>N<sub>4</sub>; engineered matrices during three heat up-cool down cycles between 293 and 1523 K. The literature data for SiC is also shown in the figure for comparison [28].

heating and cooling cycles. The fact that the  $\Delta L/L_0$  values are lower for the CrSi<sub>2</sub>-EM than SiC suggests that compressive residual stresses are likely to be present in the matrix at room temperature, which should enhance room temperature fracture strength of the matrix. Similar thermal expansion behavior is observed for the CrMoSi-EM specimen (Figure 21(b)). Figure 21(c) shows the thermal expansion values for 10%MoSi<sub>2</sub>-70%SiC-20%Si<sub>3</sub>N<sub>4</sub> (MoSi<sub>2</sub>-EM), where the composition of the original material used to generate the data shown in Figure 19 was reformulated. On the first heat-up cycle, the material exhibited a large thermal expansion. However, after the material was reheated again and thermally cycled between 293 and 1523 K, the magnitudes of  $\Delta L/L_0$  match those of SiC almost exactly. As shown in Figure 22, the specimen had developed several circumferential and longitudinal cracks on the surface during the thermal expansion measurements. Owing to the potential thermal instability of this material during thermal cycling, the MoSi<sub>2</sub>-EM was no longer considered for further development. The thermal expansion responses for the TiSi<sub>2</sub>-EM (Figure 21(d)) and WSi<sub>2</sub>-EM (Figure 21(e)) were similar to the observations on the CrSi<sub>2</sub>-EM matrix (Figure 21(a)). Once again, the thermal expansions for these

engineered matrices match those of SiC very closely and do not exhibit any significant change during thermal cycling.

It is clear from Figure 21 that except for MoSi<sub>2</sub>-EM, which exhibited thermal instability during the first heat-up cycle, all other engineered matrices show little change in the magnitudes of  $\Delta L/L_0$  during the heat-cool cycles. Noting that these matrices were formulated using the concepts described in Section 2.3, it is remarkable that the magnitudes of  $\Delta L/L_0$  are very close to those for SiC [28] as predicted by Equation (3) (Figure 23). These observations provide a complete proof of the proposed concept of ensuring thermal compatibility between the engineered matrix and the SiC fibers postulated in item (d) of Section 2.0.

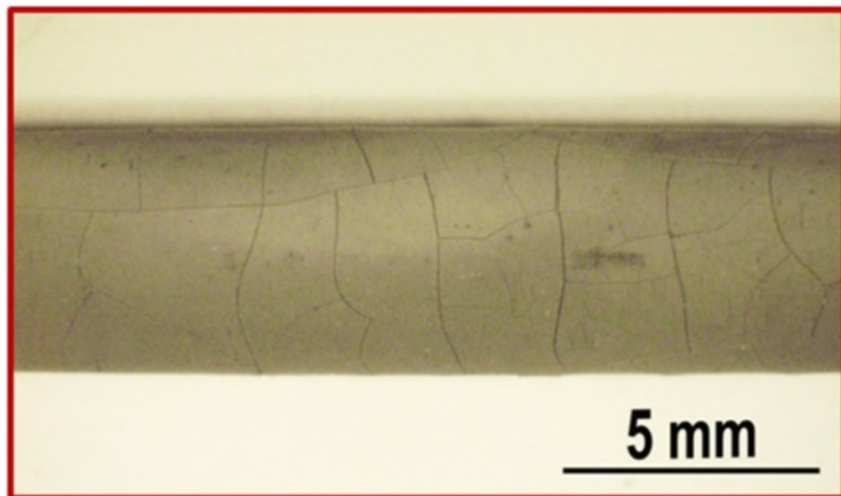


Figure 22.—Macrograph of the 10%MoSi<sub>2</sub>-70%SiC-20%Si<sub>3</sub>N<sub>4</sub> specimen after thermally cycling between 293 and 1523 K showing several longitudinal and circumferential cracks.

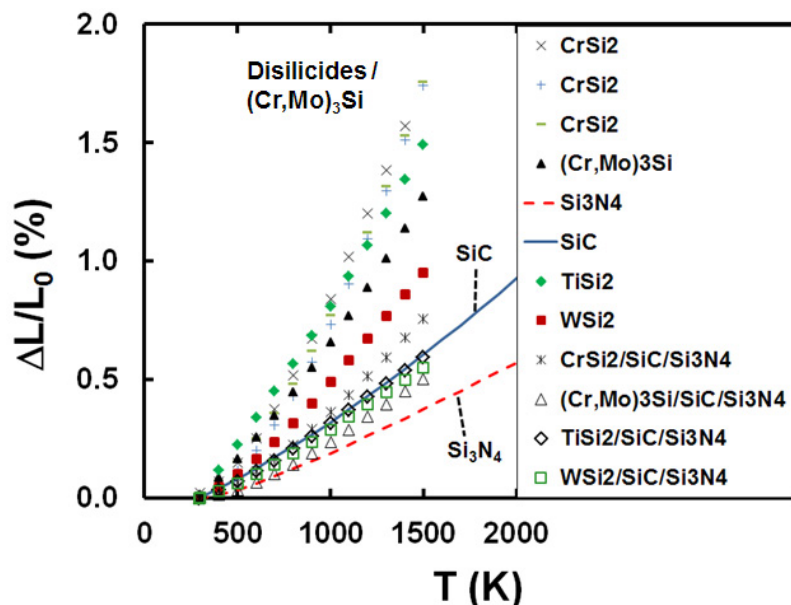


Figure 23.—Comparison of the temperature dependence of the thermal strains for disilicides, CrMoSi, engineered matrices with those for SiC [28] and Si<sub>3</sub>N<sub>4</sub> [28].



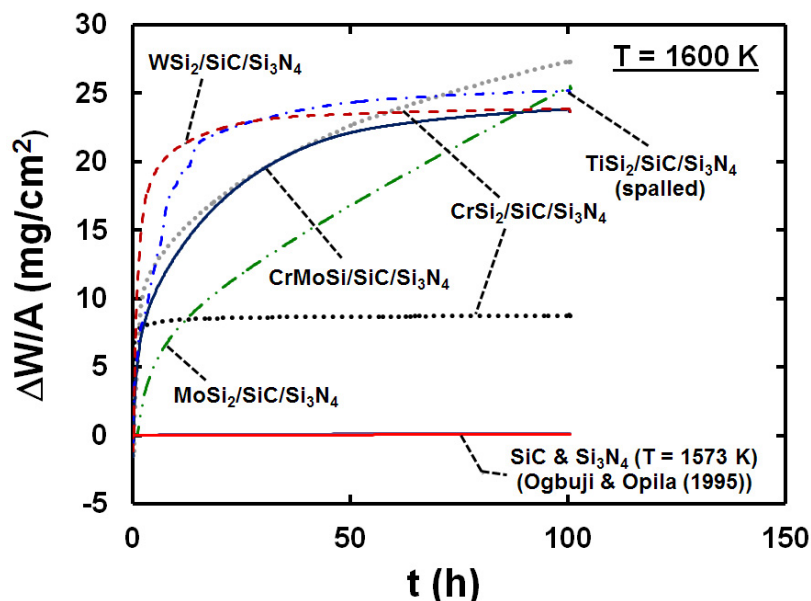


Figure 24.—Comparison of the isothermal oxidation behavior of several engineered matrices with those for SiC [43] and Si<sub>3</sub>N<sub>4</sub> [43] showing the change in the specific weight change with oxidation time.

## 4.2 Isothermal Oxidation Behavior of Engineered Matrices

Figure 24 compares the isothermal oxidation behaviors of CrSi<sub>2</sub>-EM, CrMoSi-EM, MoSi<sub>2</sub>-EM, TiSi<sub>2</sub>-EM and WSi<sub>2</sub>-EM, at 1600 K, where the weight change,  $\Delta W$ , per unit area,  $A$ , is plotted against oxidation time,  $t$ . The isothermal oxidation behavior of CVD SiC [43] and Si<sub>3</sub>N<sub>4</sub> [43] at 1573 K are shown for comparison. In contrast to SiC and Si<sub>3</sub>N<sub>4</sub>, the engineered matrices oxidize at a much higher rate, which suggests that these matrices would be able to easily getter any oxygen that infiltrates the composite matrix therefore adding an additional layer of protection for the BN-coated SiC fibers.

The engineered matrices oxidize rapidly on heating in air as the silicides begin to form a metallic oxide layer. However, as the more protective silica layer begins to form, the oxidation rate slows down in accordance with the parabolic oxidation kinetic law. An examination of Figure 24 reveals that the initial oxidation rates for TiSi<sub>2</sub>-EM and WSi<sub>2</sub>-EM are higher than those for CrSi<sub>2</sub>-EM, CrMoSi-EM and MoSi<sub>2</sub>-EM but the magnitudes of specific weight gain,  $\Delta W/A$ , for these engineered matrices are similar at  $t = 100$  h. Curiously, the oxidation rates for the two CrSi<sub>2</sub>-EM specimens were quite different, where one of the specimens exhibited relatively little specific weight gain after the initial oxidation while the other specimen continued to gain weight even after 100 h. This difference in behavior is attributed to an inhomogeneous distribution of the CrSi<sub>2</sub> particles. Since the TiSi<sub>2</sub>-EM spalled after 100 h, this matrix composition was eliminated from further consideration in the investigation.

## 4.3 Bend Properties of Engineered Matrices

As postulated in item (a) Section 2.0 and discussed in Section 2.1, increasing the local plasticity of the matrix should result in an increase in the strength of the matrix as the crack tip is blunted and the fracture toughness of the material increases. Figure 25 shows the bend stress-strain curves for the CrSi<sub>2</sub>-EM between room temperature and 1588 K. On close examination, it is evident that the bend strength increases with increasing temperature above 898 K corresponding to an increase in plasticity of the material. Above 1273 K, general plasticity increases and the strength decreases as the material deforms readily. However, the specimen tested at 1588 K exhibits the highest strength presumably because of the dominance of local plasticity over general plasticity which serves to blunt the crack. The advent of local plasticity rather than general plasticity is attributed to an inhomogeneous distribution of the CrSi<sub>2</sub>



particles. Clearly, designing the matrix in order to enhance local plasticity while reducing the advent of general plasticity would be advantageous in a composite.

Figure 26 shows the four-point bend stress-strain curves for the CrMoSi-EM matrix. Once again, the bend strength increases with increasing temperature up to 1573 K as the plasticity of the material increases. Above 1573 K, the strength drops at the higher temperatures although the data does not vary in a consistent manner with increasing temperature. The reason for a lack of a consistent trend is unclear. Nevertheless, the results shown in Figure 26 are consistent with the discussion in Section 2.0 that increasing the local plasticity of the matrix results in a corresponding increase in its strength.

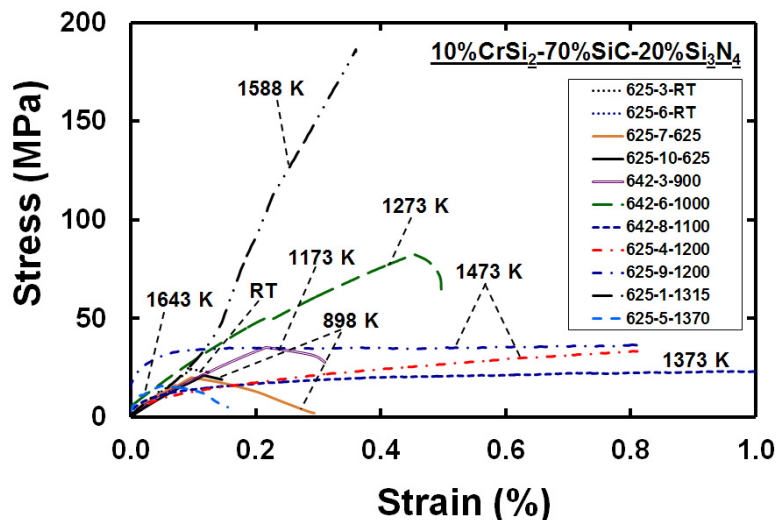


Figure 25.—Four-point bend stress-strain curves for 10%CrSi<sub>2</sub>-70%SiC-20%Si<sub>3</sub>N<sub>4</sub> tested in air between room temperature (RT) and 1588 K showing that the bend strength increases with increasing temperature due to an increase in plasticity.

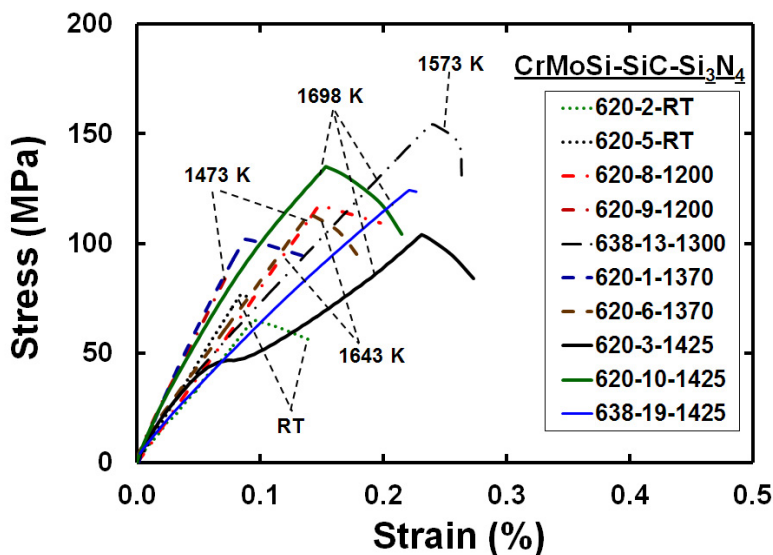


Figure 26.—Four-point bend stress-strain curves for 10%CrMoSi-60%SiC-30%Si<sub>3</sub>N<sub>4</sub> tested in air between room temperature (RT) and 1698 K showing that the bend strength increases with increasing temperature due to an increase in plasticity.

High temperature four point bend stress-strain data could not be determined for the  $\text{WSi}_2$ -EM since the specimens catastrophically oxidized (i.e., “pest”) and crumbled to powder during heat-up to test temperature. This catastrophic oxidation is due to the fact that the microstructure unexpectedly contained W-rich particles (Figure 15 and Figure 16). Therefore, this engineered matrix was dropped from further consideration in this investigation.

Based on the bend, isothermal oxidation and thermal expansion results discussed earlier, the  $\text{CrSi}_2$ -based and  $\text{CrMoSi}$ -based compositions were down selected for further development for 1588 (2400 °F) and 1755 K (2700 °F) composite matrix applications, respectively.

#### 4.4 Composite Fabrication Trials

As mentioned in Section 3.3, attempts to fabricate EMCs with a high and well distributed engineered matrix and minimizing the void volume fraction in the preforms to a minimum has not been completely successful. More research and development is continuing under the Aerosciences Project and the current description relates to the outcome of research conducted under Phases I and II of the ARMD Seedling Program.

Infiltrating the preforms with particle slurry and silicide melt proved to be particularly challenging for several reasons. Figure 27(a) shows the top view of a Sylramic fiber-reinforced preform while Figure 27(b) shows the CT scan image of its cross-section. The void area fraction varied between 21 and 23 percent. As shown in the schematic Figure 27(c), the voids are seldom directly connected to the free surface so that complete infiltration of the preform by the particulate slurry and molten silicon or silicide to fill these cavities is difficult to achieve due to the tortuous path that the slurry and molten metal have to follow. Additionally, particles in the slurry are likely to be filtered by the woven SiC tows so that it is desirable that the particle size be small enough to be able to enter the voids and the particles be well separated and bound to the carrier medium. With both particulate slurry and melt infiltration, it is important to adjust the viscosity of the fluid and to ensure that it adequately wets the SiC fiber surface so that it penetrates the interior of the preform.

##### 4.4.1 Slurry Infiltration

The particle size distribution was determined for attrition milled 20% $\text{CrSi}_2$ -55%SiC-20% $\text{Si}_3\text{N}_4$ -5% $\text{CrB}_2$  and 22.5% $\text{CrMoSiGe}$ -49%SiC-22.5% $\text{Si}_3\text{N}_4$ -5% $\text{CrB}_2$  powders<sup>2</sup> (Figure 28). The average diameters were 0.389 and 0.530  $\mu\text{m}$ , respectively, with the maximum powder diameters being 0.611 and 0.572  $\mu\text{m}$ , respectively. For comparison, the void sizes in the preforms were typically several hundred microns. During the early stages of this investigation, the slurries were prepared by mixing ethanol and the powder, and infiltration was conducted under a mechanical pump vacuum. Although the preforms showed an increase in weight after each infiltration<sup>3</sup> (Figure 29), microstructural observations of the cross-sections of the preforms revealed that the extent of particulate infiltration was relatively small. Thus, weight change measurements of the infiltrated preforms proved to be unreliable in predicting the amount of solids loading.

Infiltration trials using powder-epoxy slurries at high pressure were more successful (Figure 30). Although the epoxy successfully completely filled the voids, the amount of particulates that could be infiltrated into the preforms was much less than the desired amount of filling about 50 percent of the void space between the woven tows. When the particulate-to-epoxy mixture ratio was increased, it was difficult to completely infiltrate the preforms (Figure 31). Even in regions where the epoxy-particulate mixture had infiltrated, the distribution of the particles was inhomogeneous (Figure 32). These observations suggest that the particles were not well separated and they were not bonded to the epoxy which effectively allowed the fibers to act as filters and separate them from the epoxy. Therefore, a considerable amount of effort was expended in trying to find a suitable binder but this effort has not been successful to date.

---

<sup>2</sup> These measurements were conducted by NanoSpense, LLC, Dayton, Ohio.

<sup>3</sup> The initial slurry infiltration trials were conducted with a 10% $\text{TiSi}_2$ -70%SiC-20% $\text{Si}_3\text{N}_4$ .

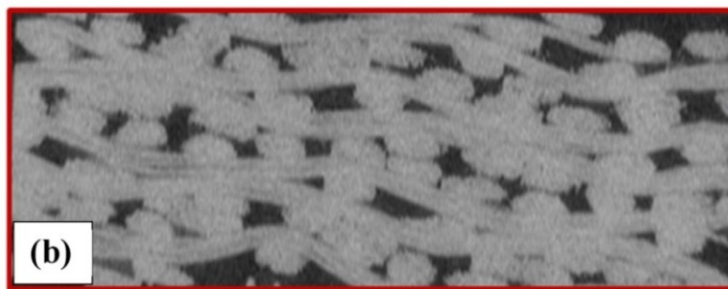
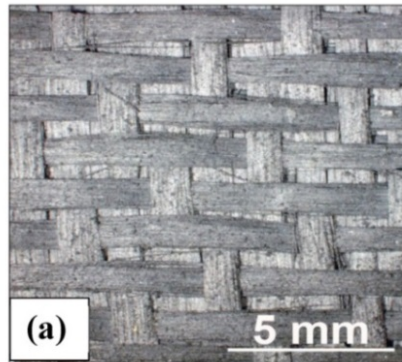


Figure 27.—(a) Optical view of the top surface of a Sylramic preform; (b) CT scan of the cross-section of the preform; and (c) schematic of the cross-section showing the distribution of voids. The area fraction of the voids was estimated by image analysis of the CT scan was 21 to 23%.

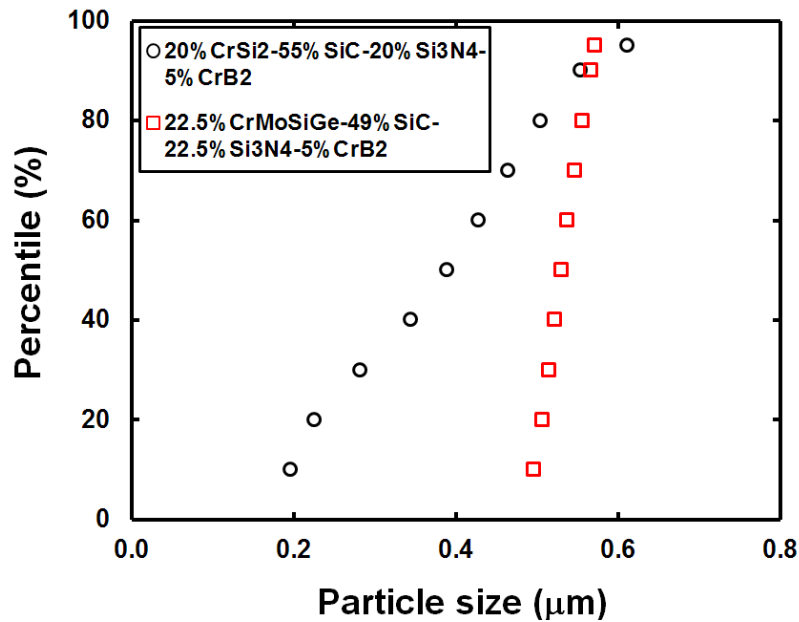


Figure 28.—Particle size distribution for attrition milled 20%CrSi<sub>2</sub>-55%SiC-20%Si<sub>3</sub>N<sub>4</sub>-5%CrB<sub>2</sub> and 22.5%CrMoSiGe-49%SiC-22.5%Si<sub>3</sub>N<sub>4</sub>-5%CrB<sub>2</sub> powders.

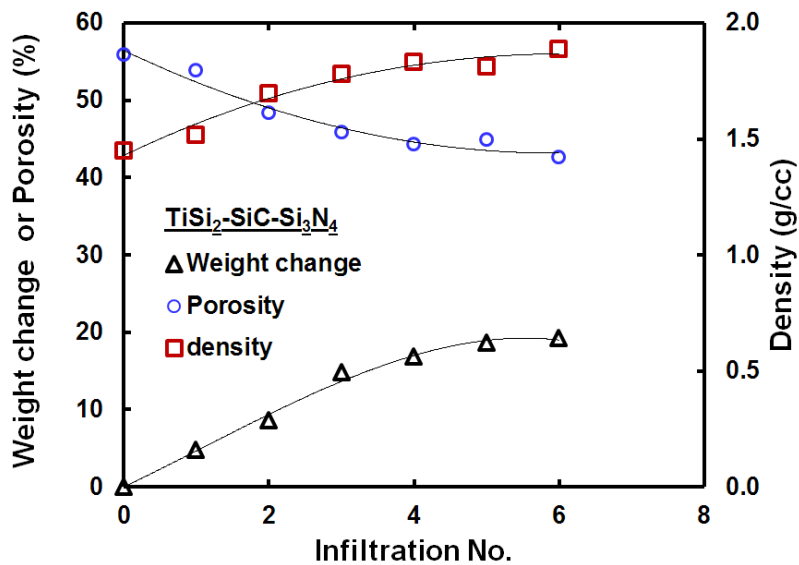


Figure 29.—Changes in the relative weight, density and estimated porosity of a Sylramic preform infiltrated with a 10%TiSi<sub>2</sub>-70%SiC-20%Si<sub>3</sub>N<sub>4</sub> powder-ethanol slurry after each infiltration trial.

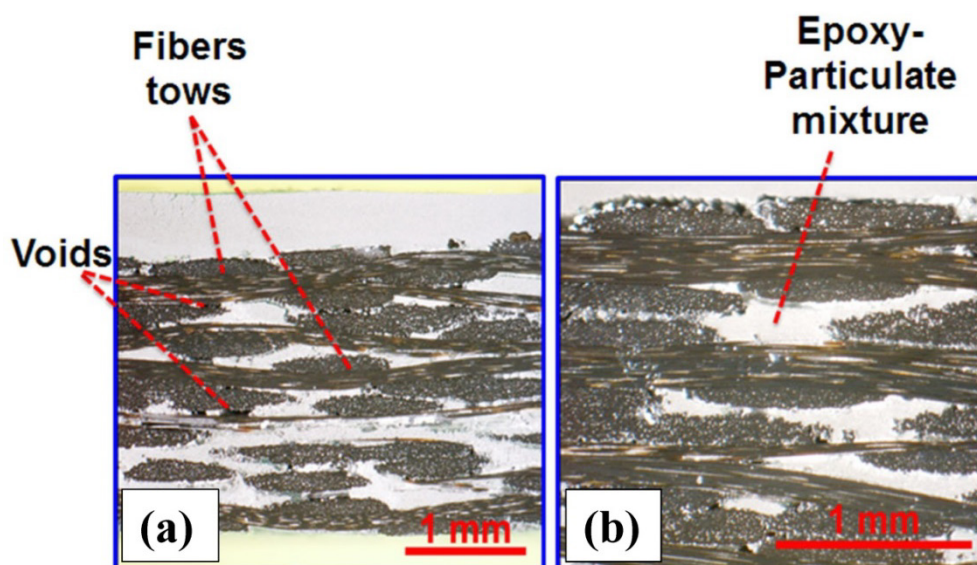


Figure 30.—Optical micrographs showing (a) low and (b) high magnification views of the cross-section of a Sylramic preform infiltrated with an epoxy-10%TiSi<sub>2</sub>-70%SiC-20%Si<sub>3</sub>N<sub>4</sub> slurry at high pressure.

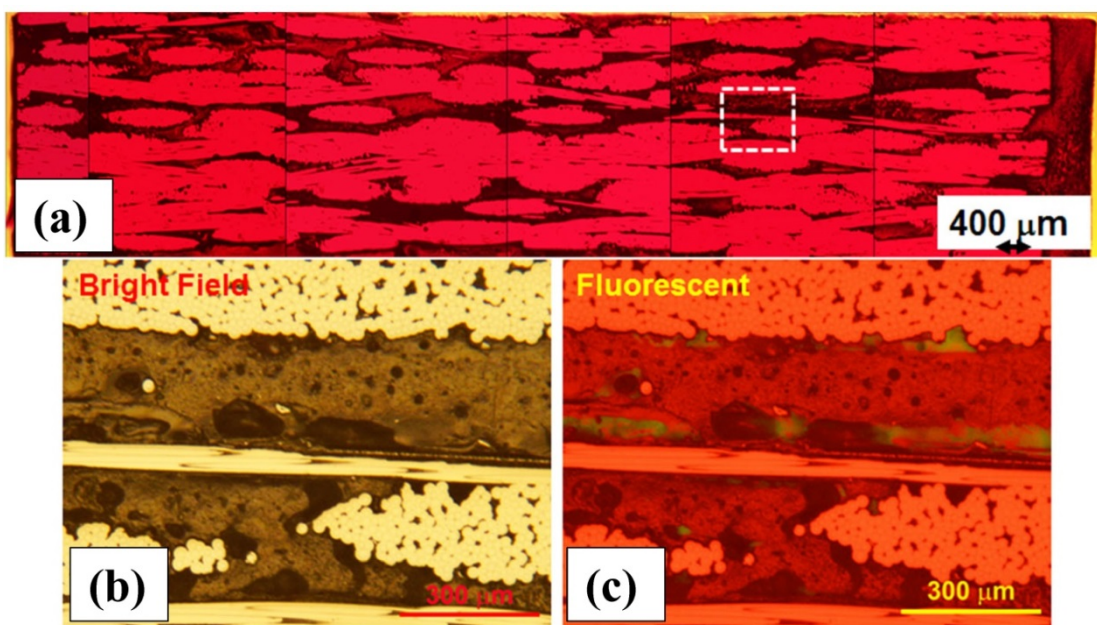


Figure 31.—Optical micrographs showing the cross-section of a Sylramic preform infiltrated with an epoxy-10%TiSi<sub>2</sub>-70%SiC-20%Si<sub>3</sub>N<sub>4</sub> slurry at high pressure. (a) Composite view of the preform cross-section in fluorescent light; (b) bright field and (c) fluorescent light views of the square region shown in (a).



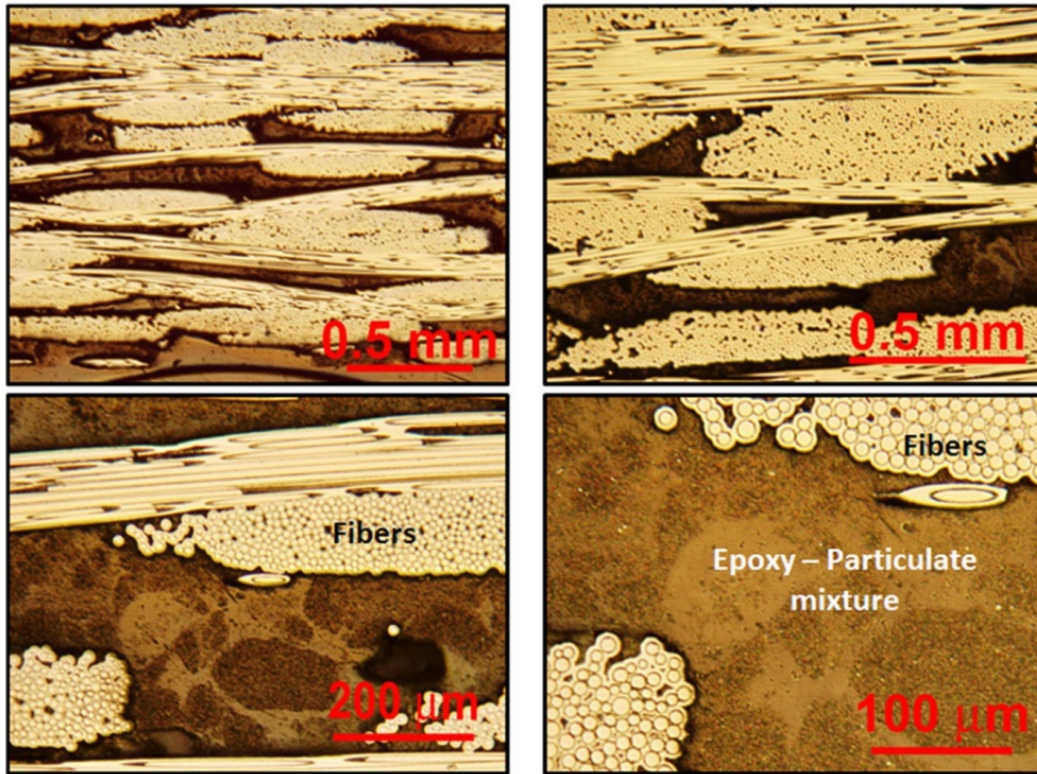


Figure 32.—Optical micrographs showing the cross-sections of a Sylramic preform infiltrated with an epoxy-10%CrMoSi-60%SiC-30%Si<sub>3</sub>N<sub>4</sub> slurry at high pressure.

In view of the fact that there is a considerable amount of research on preparing SiC [31,44,45,46,47] and Si<sub>3</sub>N<sub>4</sub> [35,44] particles dispersions in water, where the particles are well-separated due to the addition of surfactants, more recent effort has concentrated on developing aqueous-based slurries. As noted in Section 3.3, preliminary infiltration trials did not result in sufficient solids loading in the preforms. This research is currently in progress.

#### 4.4.2 Melt Infiltration

Several bend specimens, which had been infiltrated with epoxy-particulate slurry at high pressure and subsequently heated in flowing argon to pyrolyze the epoxy to carbon, were infiltrated with either Si or Si-1(at.%)Ge. Figure 33 shows the CT images, the processed images and the estimated porosity in a preform specimen at each stage of the composite fabrication process, where the red areas in the processed images represent voids. Although the CT images suggested that the area fraction of the porosity was 0.9 percent after epoxy-particulate infiltration, these images could not distinguish between the epoxy and the solids. As noted earlier, the solids loading after the epoxy-particle infiltration was low (Figure 31 and Figure 32). The porosity content after Si melt infiltration was about 1.8 percent. Figure 34 shows the microstructures of the cross-sections of the specimen, where it is clear that some regions of the preform were not infiltrated. In a second trial, where the amount of Si or Si-1(at.%)Ge was reduced, it was observed that large areas of the preform were not infiltrated (Figure 35(a) to (d)).

In order to develop a silicon-free composite matrix as postulated in item (e) in Section 2.0, melt infiltration was conducted using CrSi<sub>2</sub> and Cr-25(wt.%)Si. Figure 36 shows the Cr-Si binary phase diagram [48]. It is clear that CrSi<sub>2</sub> and Si have melting points of 1763 and 1687 K, respectively. The Cr-25(wt.%)Si has a solidus temperature of 1778 K. Thus, melt infiltrating with CrSi<sub>2</sub> and Cr-25(wt.%)Si alloys should increase the ability of the matrix to withstand temperatures higher than composites melt infiltrated with Si.

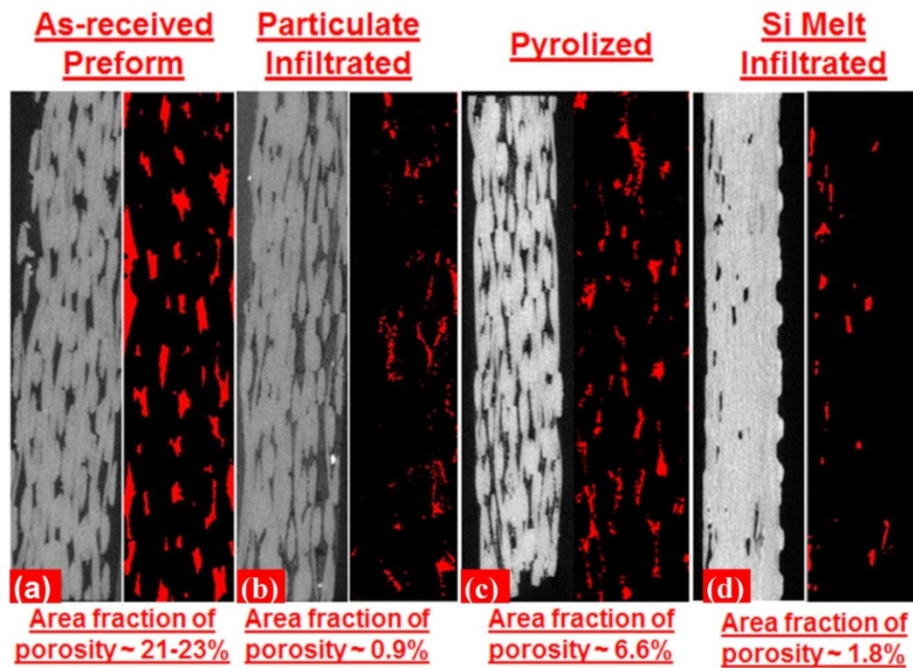


Figure 33.—CT scan (left) and processed (right) images of each stage of fabrication of an EMC. (a) As-received preform; (b) preform infiltrated with an epoxy-10%TiSi<sub>2</sub>-70%SiC-20%Si<sub>3</sub>N<sub>4</sub> slurry; (c) preform after pyrolizing the epoxy; and (d) preform after melt infiltration with silicon. The red areas in the processed images represent voids. The area fractions of the voids are shown after each processing stage.

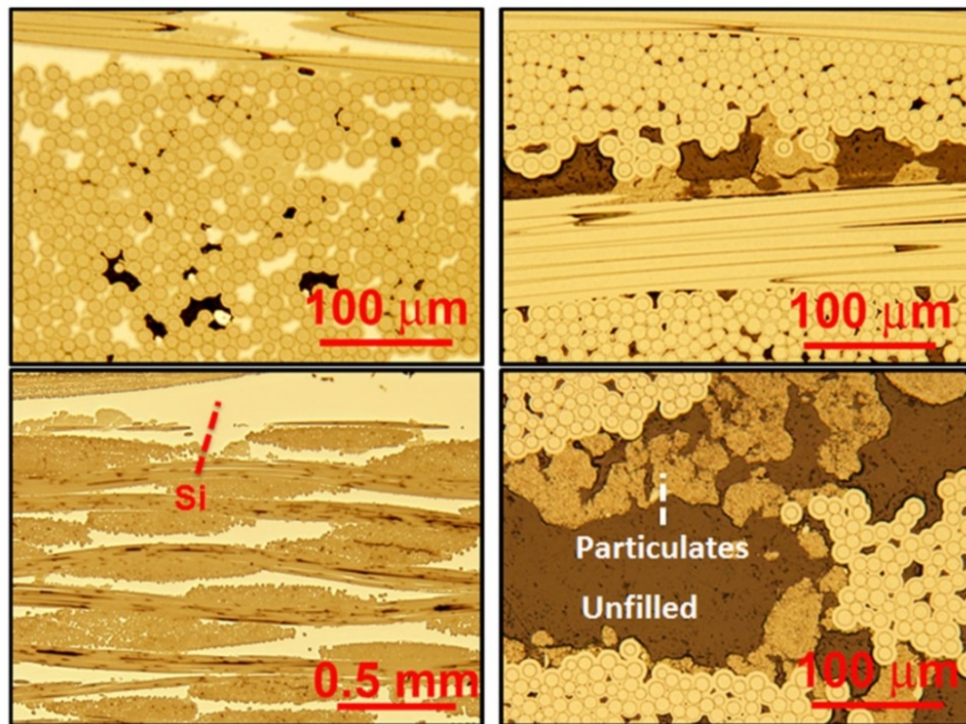


Figure 34.—Optical micrographs showing the cross-sections of a Syramic preform infiltrated with an epoxy-10%CrMoSi-60%SiC-30%Si<sub>3</sub>N<sub>4</sub> slurry and melt infiltrated with silicon.



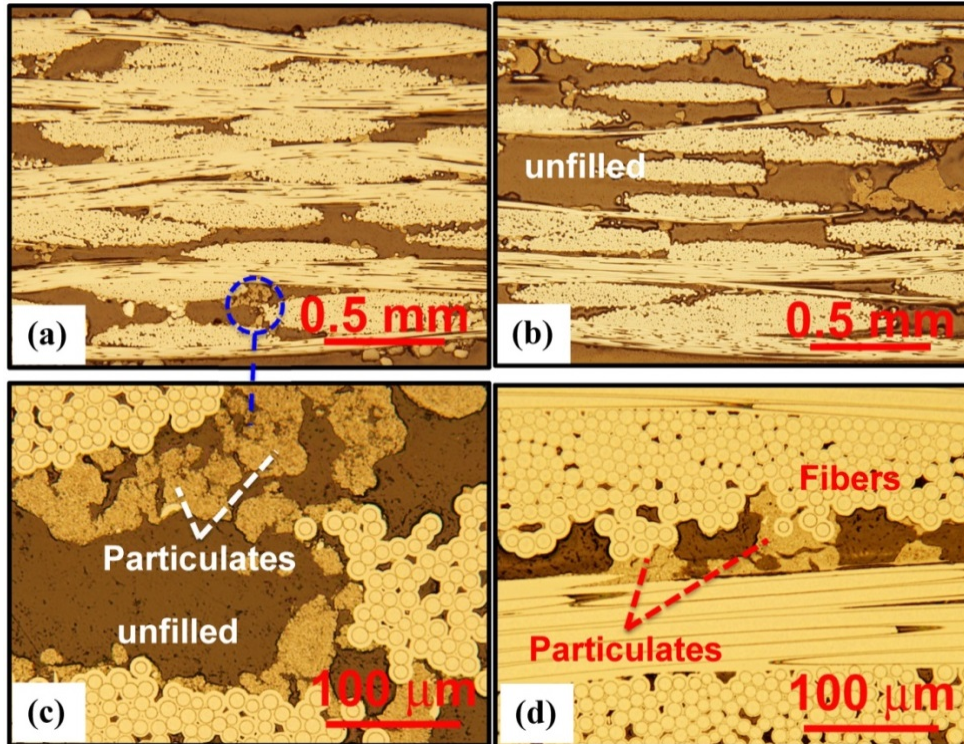


Figure 35.—Optical micrographs showing the cross-sections of Sylramic preforms infiltrated with an epoxy-90%SiC-10%Si<sub>3</sub>N<sub>4</sub> slurry and melt infiltrated with (a) and (c) silicon and (b) and (d) Si-1(at.%)Ge.

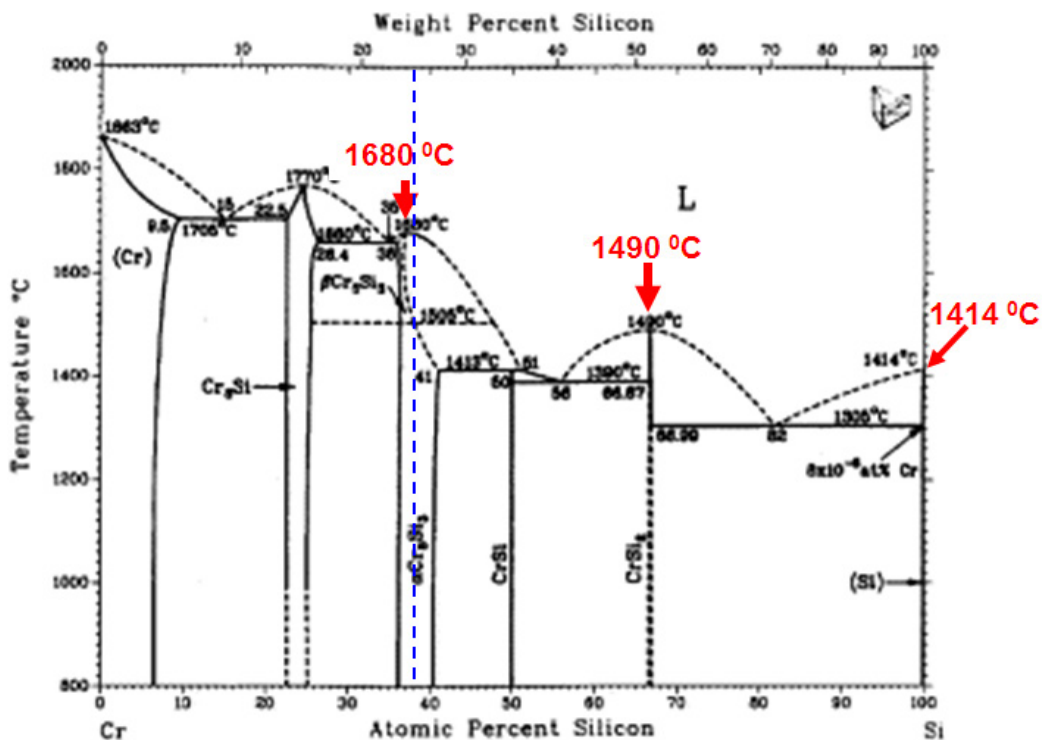


Figure 36.—Cr-Si binary phase diagram [48].



The Sylramic and Tyranno SA fibers contain  $\text{TiB}_2$  and Al present as  $\text{SiC}_{1.08}\text{Al}_{0.005}$  [49], respectively. The Sylramic fibers contain 2.3 (wt.%) B, 2.1 (wt.%) Ti and 0.8(wt.%) O [50]. The Tyranno SA fibers contain less than 2(wt.%) Al and about 0.3(wt.%) O [50,51]. Thus, it is important to verify that preforms melt infiltrated with these chromium silicides will be chemically stable both during melt infiltration as well as in the actual applications. Thermodynamic calculations using FactSage (Thermfact/CRCT (Montreal, Canada) and GTT-Technologies (Aachen, Germany)) were conducted to determine whether there would be any reactions with either the CVI SiC or the BN coatings. As shown in Table III, the thermodynamic calculations predicted that the CVI SiC and BN coatings are unlikely to be attacked by either molten  $\text{CrSi}_2$  or Cr-25%Si under an infiltration pressure of 0.1 MPa but the SiC,  $\text{Si}_3\text{N}_4$  and the silicides decompose at a lower pressure of  $1.3 \times 10^{-10}$  MPa . The decomposition of SiC under low pressures of  $1.3 \times 10^{-10}$  MPa is expected to leave a layer of carbon on the fiber surfaces readily available to react with either the molten silicides. The FactSage calculations also predicted that the presence of small amounts (0.1%) impurities, such as B, Hf, Ti and Zr, would react to form  $\text{CrB}_2$ ,  $\text{HfC}$ ,  $\text{TiSi}_2$  and  $\text{ZrC}$ , respectively, at 1808 K. While trace amounts Al were not expected to react, the thermodynamic calculations suggested that it would form liquid Al at these temperatures.

Figure 37(a) and (b) show optical micrographs of a Tyranno SA preform melt infiltrated with  $\text{CrSi}_2$  in the first trial. The preform was not completely infiltrated due to poor wetting action as evidenced by the distinct meniscus seen in Figure 37(b). A careful examination of the  $\text{CrSi}_2$ -SiC interfaces revealed that there was no reaction between the two phases (Figure 38(a) to (c)). Raman spectra from the  $\text{CrSi}_2$  matrix confirmed the absence of free C and Si, which was one of the requirements postulated in item (e) in Section 2.0. A small amount of free Si was detected in the CVI SiC coating on the fibers.

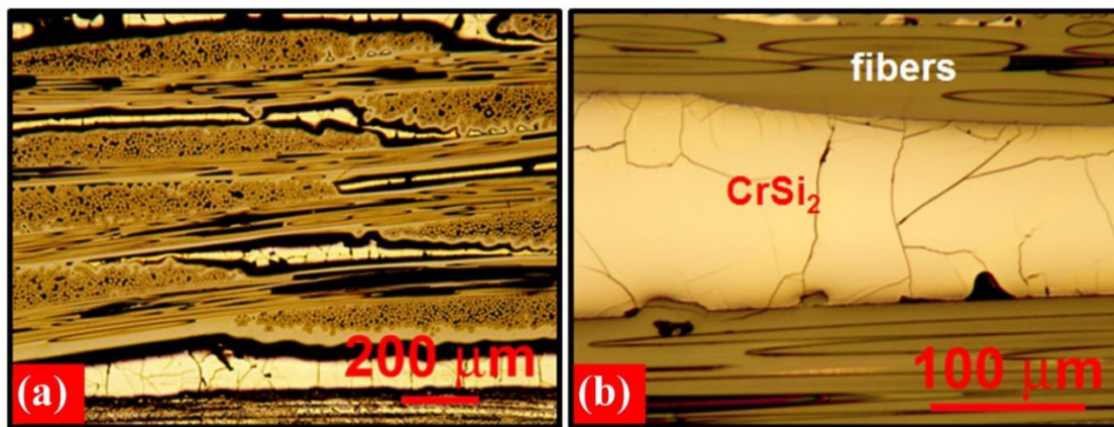


Figure 37.—(a) Low and (b) high magnification optical micrographs of the cross-section of a Tyranno SA preform melt infiltrated with  $\text{CrSi}_2$ .

TABLE III.—RESULTS FROM THE FACTSAGE CALCULATIONS

Reaction	T (K)	P (MPa)	Products	Amount (mol.)	Activity/ fugacity (MPa)	Remarks
$\beta$ -SiC (s)+ Si <sub>3</sub> N <sub>4</sub> (s)	1808	$1.3 \times 10^{-10}$	C (s) Si (g) N <sub>2</sub> (g)	0.8 3.9 2.0	1.0 $8.5 \times 10^{-11}$ $4.3 \times 10^{-11}$	SiC and Si <sub>3</sub> N <sub>4</sub> likely to decompose
$\beta$ -SiC (s)+ Si <sub>3</sub> N <sub>4</sub> (s) +CrSi <sub>2</sub> (s)	1808	$1.3 \times 10^{-10}$	C (s) Cr (g) N <sub>2</sub> (g) Si (g)	0.7 1.0 2.0 5.9	1.0 $1.4 \times 10^{-11}$ $2.3 \times 10^{-11}$ $8.5 \times 10^{-11}$	SiC and Si <sub>3</sub> N <sub>4</sub> likely to decompose
$\beta$ -SiC (s)+ Si <sub>3</sub> N <sub>4</sub> (s) +CrSi <sub>2</sub> (s)	1808	0.1	$\beta$ -SiC (s) Si <sub>3</sub> N <sub>4</sub> (s) CrSi <sub>2</sub> (s)	1.0 1.0 1.0	1.0 1.0 1.0	No reaction with SiC and Si <sub>3</sub> N <sub>4</sub>
$\beta$ -SiC (s)+Si <sub>3</sub> N <sub>4</sub> (s) CrSi <sub>2</sub> (s)+BN (s)	1808	$1.3 \times 10^{-10}$	C (s) B (g) Cr (g) N <sub>2</sub> (g) Si (g)	0.7 1.0 1.0 2.5 5.9	1.0 $1.2 \times 10^{-11}$ $1.2 \times 10^{-11}$ $3.1 \times 10^{-11}$ $7.3 \times 10^{-11}$	SiC and Si <sub>3</sub> N <sub>4</sub> likely to decompose
$\beta$ -SiC (s)+Si <sub>3</sub> N <sub>4</sub> (s) CrSi <sub>2</sub> (s)+BN (s)	1808	0.1	BN (s) $\beta$ -SiC (s) Si <sub>3</sub> N <sub>4</sub> (s) CrSi <sub>2</sub> (s)	1.0 1.0 1.0 1.0	1.0 1.0 1.0 1.0	No reaction with SiC and Si <sub>3</sub> N <sub>4</sub>
$\beta$ -SiC (s)+ Si <sub>3</sub> N <sub>4</sub> (s) CrMoSi (s)+CrSi <sub>2</sub> (s) +BN	1808	$1.3 \times 10^{-10}$	C (s) MoB (s) Cr (g) N <sub>2</sub> (g) Si (g)	0.7 0.3 1.4 2.5 6.1	1.0 1.0 $1.7 \times 10^{-11}$ $3.0 \times 10^{-11}$ $7.3 \times 10^{-11}$	Reaction of Mo and BN; SiC and Si <sub>3</sub> N <sub>4</sub> likely to decompose
$\beta$ -SiC (s)+ Si <sub>3</sub> N <sub>4</sub> (s) CrMoSi (s)+CrSi <sub>2</sub> (s) +BN	1808	0.1	BN (s) $\beta$ -SiC (s) Si <sub>3</sub> N <sub>4</sub> (s) CrSi <sub>2</sub> (s) Cr <sub>5</sub> Si <sub>3</sub> (s) MoSi <sub>2</sub> (s)	1.0 1.1 1.0 0.5 0.2 0.3	1.0 1.0 1.0 1.0 1.0 1.0	No reaction with SiC and Si <sub>3</sub> N <sub>4</sub>

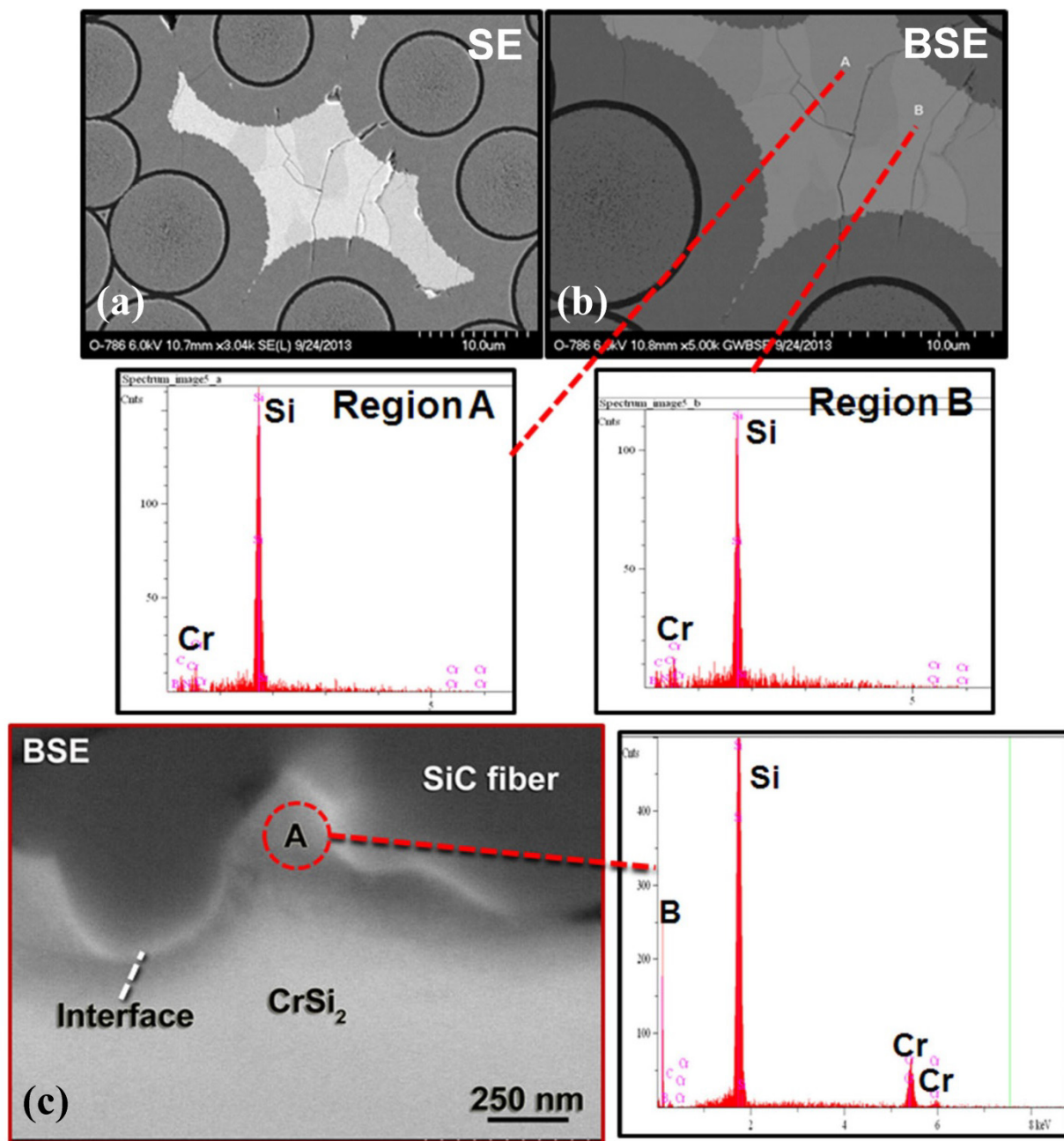


Figure 38.—(a) Scanning electron and (b) and (c) back scattered electron images of the cross-section of a Tyranno SA preform melt infiltrated with CrSi<sub>2</sub>. The corresponding energy dispersive spectra confirm that there was no reaction between the CrSi<sub>2</sub> and SiC.

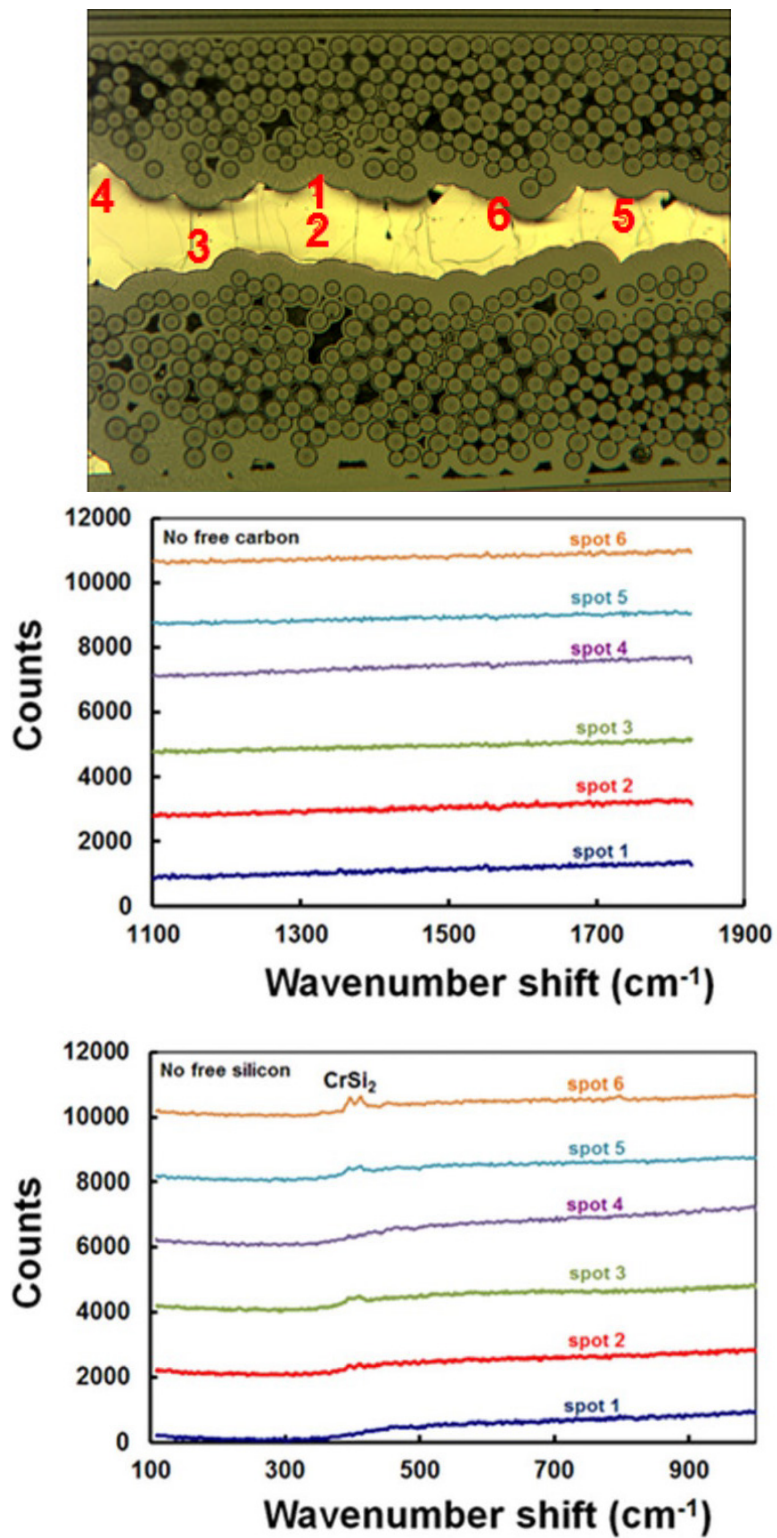


Figure 39.—Raman spectra for C and  $\text{CrSi}_2$  from regions 1 to 6 identified in the optical micrograph above demonstrating the absence of free C and Si.

Since the results from the first  $\text{CrSi}_2$  melt infiltration trials were encouraging, subsequent trials were conducted at higher temperatures and longer times in order to increase the fluidity of the silicide and improve the degree of infiltration of the preforms. However, an examination of the microstructures showed considerable evidence that the fibers had been attacked during melt infiltration (Figure 40 and Figure 41). Energy dispersive spectroscopy from four areas of Sylramic preforms revealed the following (Figure 40): The EDS pattern from Region A showed a large Si peak with much smaller B and Cr peaks; well-defined B and Ti peaks as well as a diffused Si peak are observed in Region B; Region C shows only a large Si peak; and Region D within the fiber shows only Ti and Si peaks. Surprisingly, except in Region A, Cr peaks are largely absent from the other regions. Similarly, the Tyranno SA preform in a second melt infiltration trial showed evidence of reaction with the fiber CVI SiC and BN coatings (Figure 41). Figure 40 and Figure 41 suggest that the  $\text{CrSi}_2$  has reacted with the CVI SiC and the BN coatings, which is inconsistent with the thermodynamic predictions detailed in Table III. The exact reason for this inconsistency is unclear and it is being investigated further.

#### 4.5 Bend Properties of Engineered Matrix Composites

Figure 42 and Figure 43 compare the four-point bend stress-strain curves for several Sylramic composites with and without  $\text{CrMoSi}$  at room temperature and 1645 K, respectively. Data for an uninfiltreated preform are included for baseline comparisons. These composites were first slurry infiltrated with either 90%SiC-10% $\text{Si}_3\text{N}_4$  or 10% $\text{CrMoSi}$ -80%SiC-10% $\text{Si}_3\text{N}_4$  and then melt infiltrated with either Si or Si-1(at.%)Ge. Not surprisingly, the composites are stronger than the preforms. However, as discussed in Section 4.4.2, the voids in these composites were not completely filled (Figure 34 and Figure 35). Therefore, the data shown in Figure 42 and Figure 43 must be interpreted with a certain degree of caution.

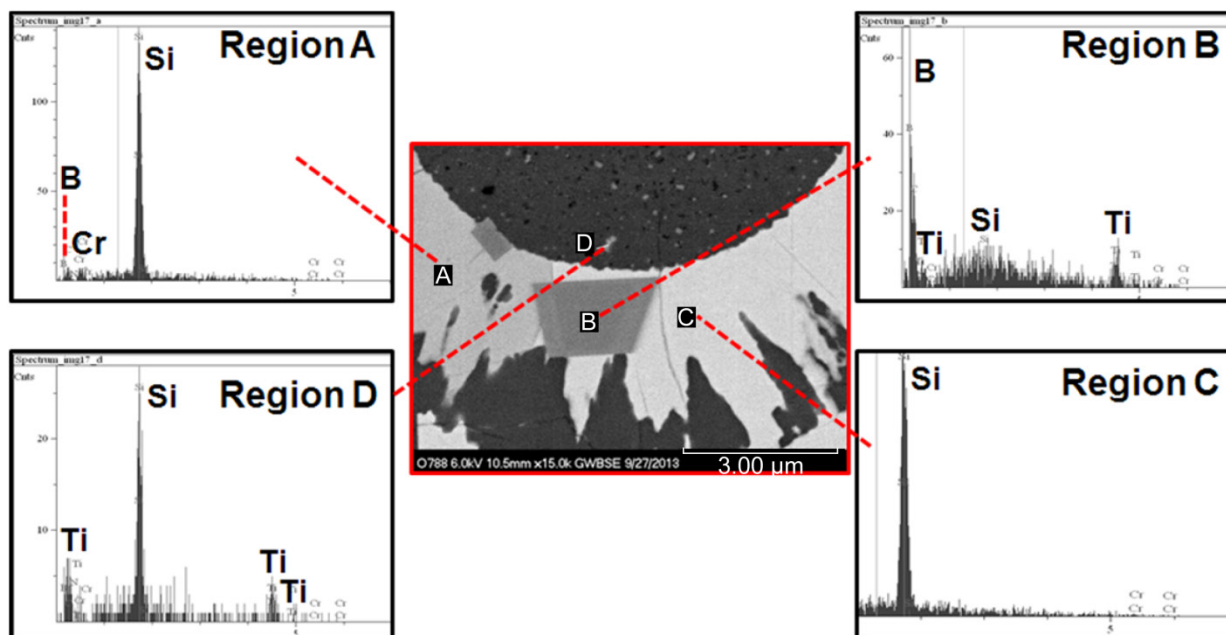


Figure 40.—Back-scattered electron image and energy dispersive spectra from Regions A, B, C and D for a Sylramic preform melt-infiltrated with  $\text{CrSi}_2$ .



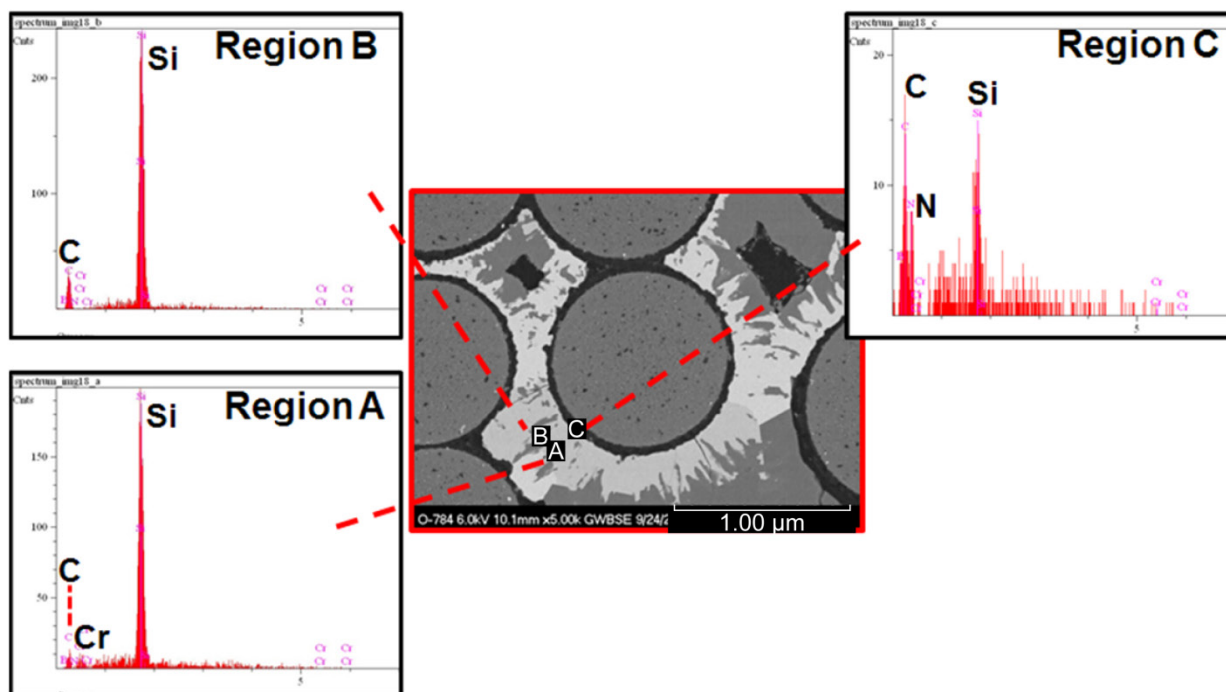


Figure 41.—Back-scattered electron image and energy dispersive spectra from Regions A, B and C for a Tyranno SA preform melt-infiltrated with  $\text{CrSi}_2$ .

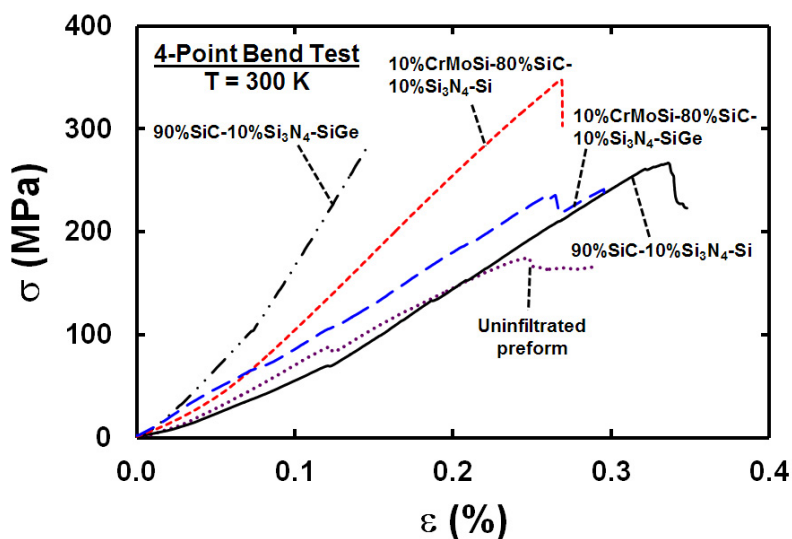


Figure 42.—Room temperature four-point bend tests for engineered matrix composites comparing the effects of Ge and CrMoSi additions.

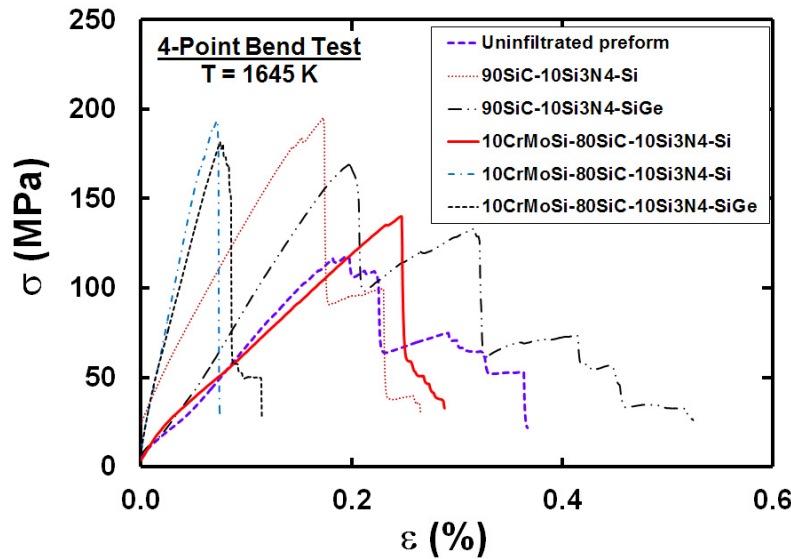


Figure 43.—Four-point bend tests for engineered matrix composites comparing the effects of Ge and CrMoSi additions at 1645 K.

#### 4.6 Self-Healing Studies

Composite specimens were pre-cracked and oxidized as discussed in Section 3.4.5. These specimens were re-tested in four-point bend tests at 1645 K. Figure 44(a) to (d) compare the bend stress-strain curves for these specimens with those shown in Figure 43. These preliminary studies revealed that the bend strengths of the pre-cracked specimens significantly increased in almost all instances after oxidation.

Initial assessment of additives on the self-healing characteristics of engineered matrices revealed that they were effective in healing scratches and closing a 1 mm diameter hole to various degrees. After oxidation at 1600 K for 24 h, CrMoSi-SiC specimen without any additives showed no significant healing of the scratches and the hole (Figure 45(a)). However, adding 5(wt.%) CrB<sub>2</sub> had a significant effect on healing the scratches and partially closing the hole (Figure 45(b)). Continued oxidation at 1700 K for a cumulative oxidation time of 100 h showed that the hole on the exposed top face had significantly closed relative to that on the rear face (Figure 46(a) to (d)). The presence of 1(wt.%)Ge in the CrMoSi alloy as a solid solution was fairly effective in healing the scratches, but it had a smaller effect on closing the hole (Figure 45(c)). The amount of Y in the CrMoSi alloy was 0.1 wt.%, which was insufficient to significantly heal the scratches (Figure 45(d)). The addition of 5(wt.%) ZrSiO<sub>4</sub> was quite effective in healing the scratches although the hole showed good closure, the oxide scale was layered and brittle.

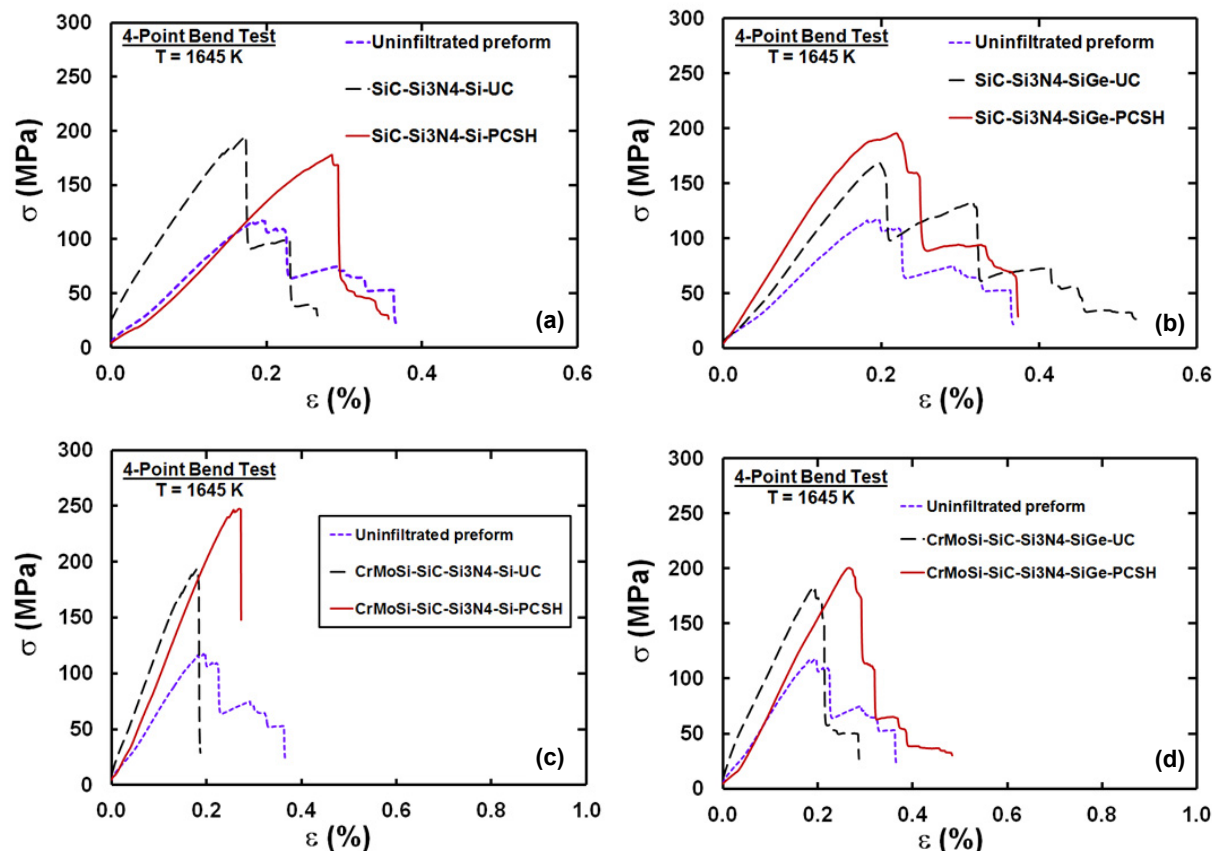


Figure 44.—Four-point bend tests for engineered matrix composites at 1645 K comparing the effects of self-healing experiments. (a) 90(wt.%) SiC-10%Si<sub>3</sub>N<sub>4</sub>-Si; (b) 90(wt.%) SiC-10%Si<sub>3</sub>N<sub>4</sub>-SiGe; (c) 10(wt.%) CrMoSi-80% SiC-10%Si<sub>3</sub>N<sub>4</sub>-Si; (d) 10(wt.%) CrMoSi-80% SiC-10%Si<sub>3</sub>N<sub>4</sub>-SiGe.

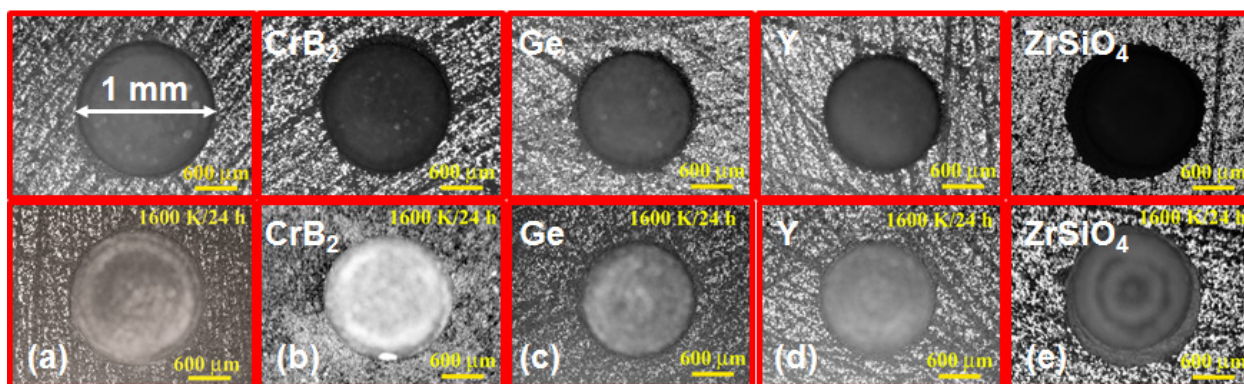


Figure 45.—Comparison of the effective of additives on the self-healing of scratches and a 1 mm diameter hole before and after oxidation at 1600 K for 24 h. (a) 20(wt.%)CrMoSi-80%SiC; (b) 20%CrMoSi-75%SiC-5%CrB<sub>2</sub>; (c) 20%CrMoSiGe-80%SiC; (d) 20%CrMoSiY-80%SiC; and (e) 20%CrMoSi-75%SiC-5%ZrSiO<sub>4</sub>.



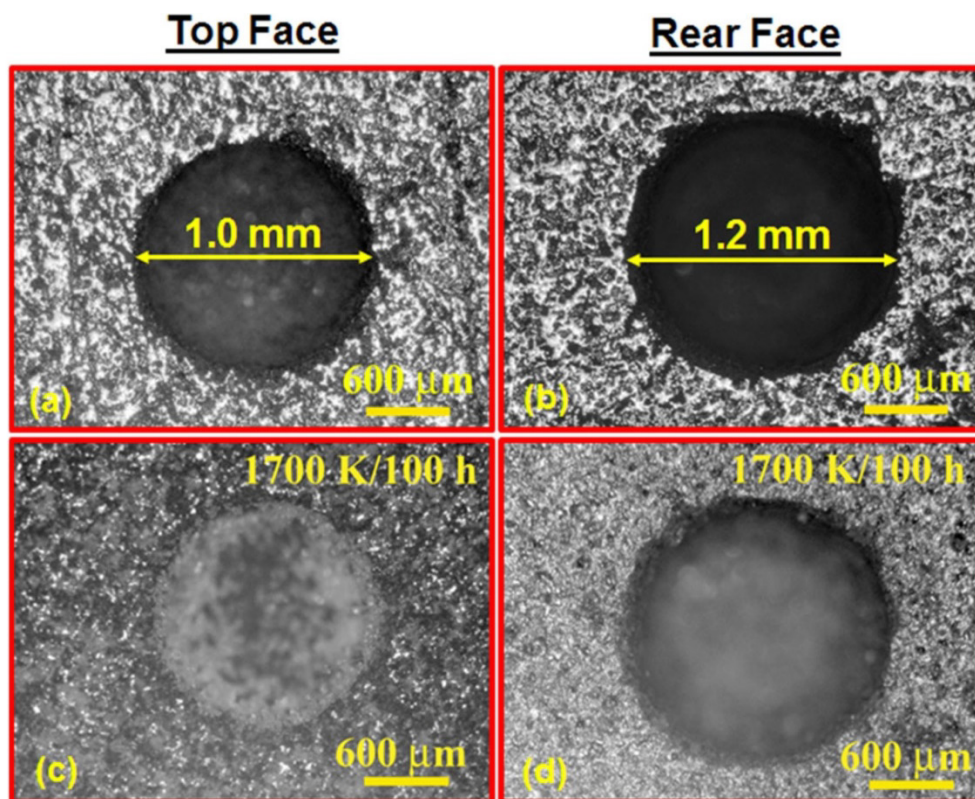


Figure 46.—Optical macrographs showing (a) and (c) the top face exposed to air and (b) and (d) the rear face on the tray bottom showing the extent of hole closure after oxidation of a 20%CrMoSi-75%SiC-5%CrB<sub>2</sub> at 1700 K for 100 h. Views of the holes (a) and (b) before oxidation; and (c) and (d) after oxidation.

Energy dispersive spectra of the oxide scales formed on these specimens after oxidation at 1700 K for a cumulative oxidation time of 100 h revealed that they were silica (Figure 47 to Figure 50). However, the morphology of the scale was influenced by the additive. Without any additives, the morphology of the scale was granular (Figure 47). Silica globules were observed with the addition of 5(wt.%) CrB<sub>2</sub> (Figure 48). In contrast, Ge addition resulted in a “mud flat” scale morphology thereby suggesting a low viscosity scale, which would be advantageous in filling cracks (Figure 49). The effect of Y on the scale was similar to that shown in Figure 47 but with more rounded and fused features (Figure 50). The specimen with ZrSiO<sub>4</sub> resulted in catastrophic oxidation at 1700 K.

Similarly, 5(wt.%) CrB<sub>2</sub> and 5(wt.%) ZrSiO<sub>4</sub> additions to 20(wt.%) CrSi<sub>2</sub>-75%SiC were effective in partially closing a 1 mm diameter hole, where the scale for the specimen with ZrSiO<sub>4</sub> was brittle (Figure 51(a) to (d)). The relative change in the hole dimensions,  $\Delta d/d_0 = (d_f - d_0)/d_0$ , where  $d_f$  and  $d_0$  are the final and initial diameters of the hole, significantly decreased with the addition of 5(wt. %) of either CrB<sub>2</sub> or ZrSiO<sub>4</sub> (Figure 52(a) and (b)). For example, the hole dimensions closed by about 60% for CrMoSi/SiC oxidized at 1700 K for 100 h. However, specimens with ZrSiO<sub>4</sub> suffered catastrophic oxidation and the specimens fell apart.

Notched specimens from compositions identical to the specimens shown in Figure 45(b) to (d) were isothermally oxidized at 1700 K for 24 h. Figure 53 shows examples of micrographs of the oxidized and unoxidized notches for CrMoSi-SiC-1(wt.%) CrB<sub>2</sub> (Figure 53(a) and (c)) and CrMoSi-SiC-5(wt. %) CrB<sub>2</sub> (Figure 53(b) and (d)), where it is evident that the surfaces have undergone extensive oxidation for the specimens with a 5 (wt. %) addition of CrB<sub>2</sub>.

Additional compositions were prepared based on the results shown in Figure 45 to Figure 53 with additions of sufficient amounts of Si<sub>3</sub>N<sub>4</sub> to compensate for the thermal expansion of CrSi<sub>2</sub> and CrMoSi. Figure 54 and Figure 55 show the micrographs, energy dispersive spectra and elemental x-ray maps for one of these new compositions, which are currently being investigated for self-healing properties. The microstructures showed a lot of porosity (Figure 54). The magnitudes of E<sub>MOD</sub> measured for several specimens with a composition of 25(wt. %)CrMoSi-45%SiC-25Si<sub>3</sub>N<sub>4</sub>-5%CrB<sub>2</sub> increased after they were annealed in air at 1698 K for 1800 s compared to those annealed in argon under identical conditions (Figure 56). The average values of E<sub>MOD</sub> for the as-received and specimens annealed in argon were 75 ± 4.1 GPa and 72.4 ± 4.7 GPa, respectively. In comparison, the average value for the specimens annealed in air was 112 ± 4.5 GPa, which represents a 49 percent increase over the as-received values. As shown in Figure 56, there was a corresponding increase in the densities of the specimens with the average value increasing from 2.62 to 2.80 g/cc for specimens annealed in argon and air, respectively. Fracture toughness tests conducted on SEVNB specimens annealed in air and argon at 1698 K for 1800 s were 3.3 and 1.6 MPa•√m, respectively. These observations are consistent with the self-healing of the voids in the specimens. Microstructural analyses will be performed on these specimens to confirm this hypothesis.

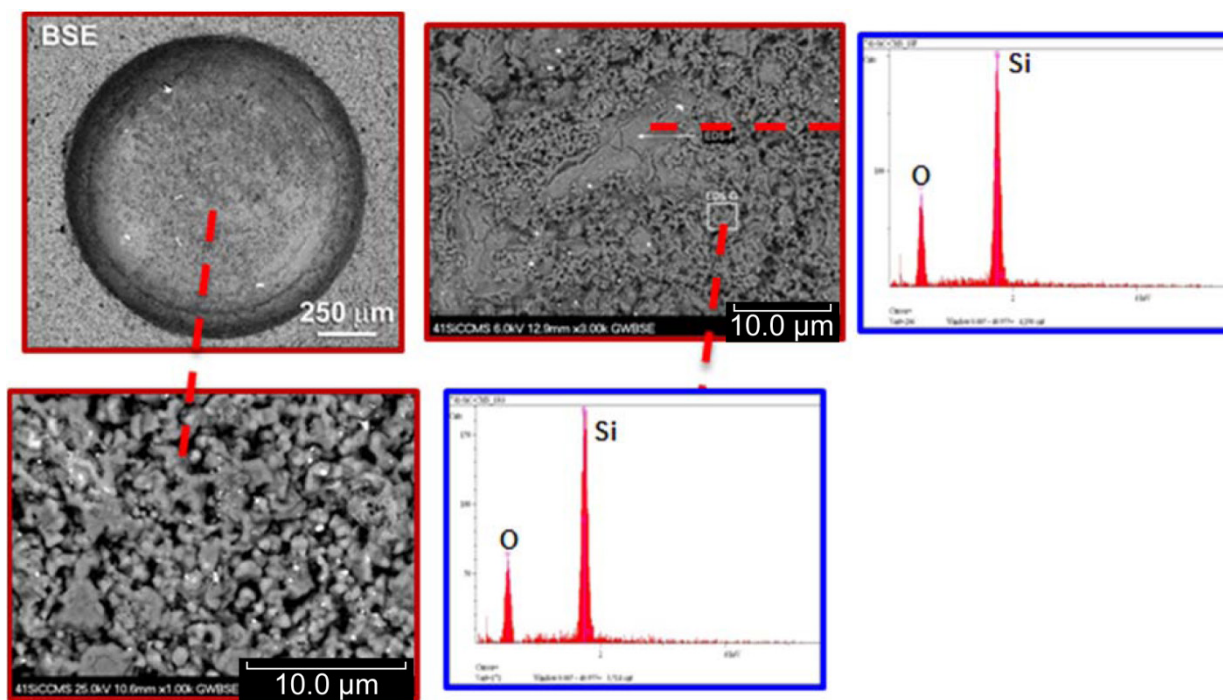


Figure 47.—Back-scattered electron images and energy dispersive spectra of the silica scale formed on 20(wt.%)CrMoSi-80%SiC after oxidation at 1700 K for a cumulative oxidation time of 100 h.

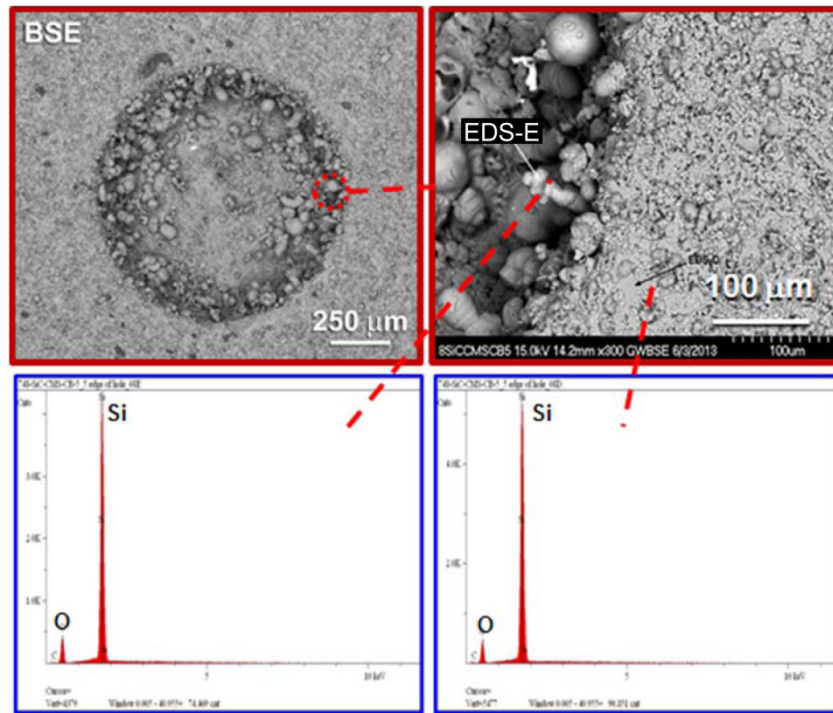


Figure 48.—Back-scattered electron images and energy dispersive spectra of the silica scale formed on 20%CrMoSi-75%SiC-5%CrB<sub>2</sub> after oxidation at 1700 K for a cumulative oxidation time of 100 h.

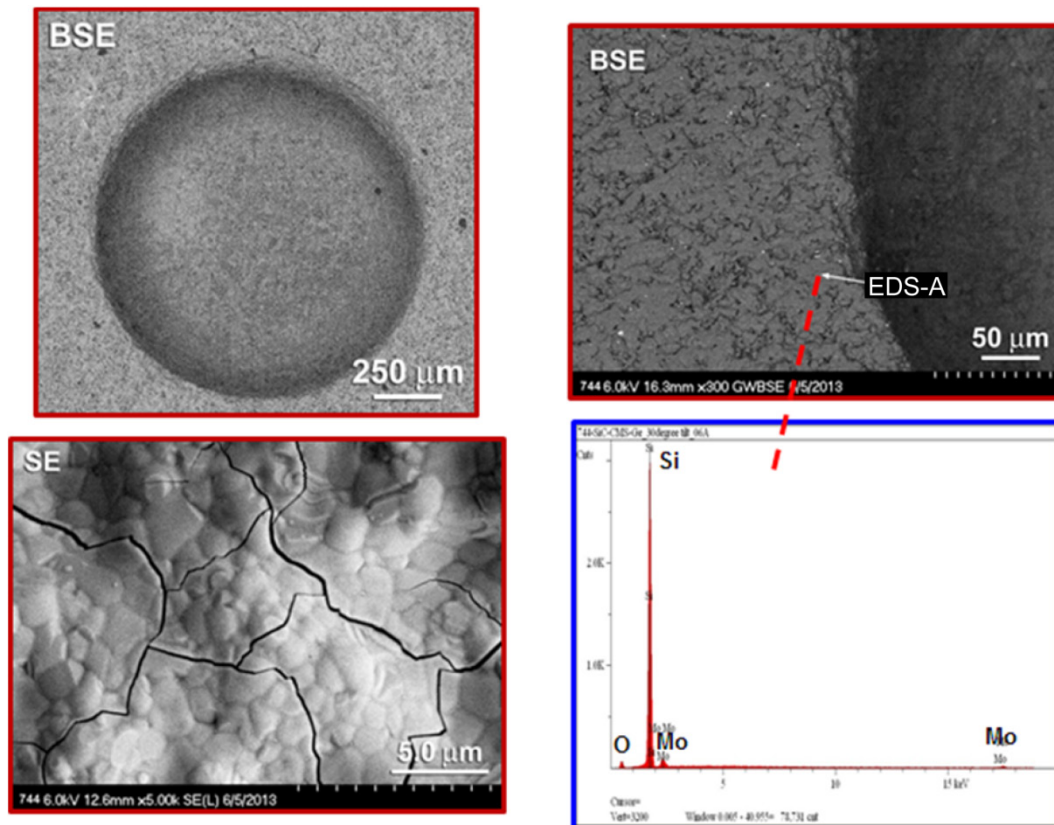


Figure 49.—Back-scattered electron images and energy dispersive spectra of the silica scale formed on 20%CrMoSiGe-80%SiC after oxidation at 1700 K for a cumulative oxidation time of 100 h.



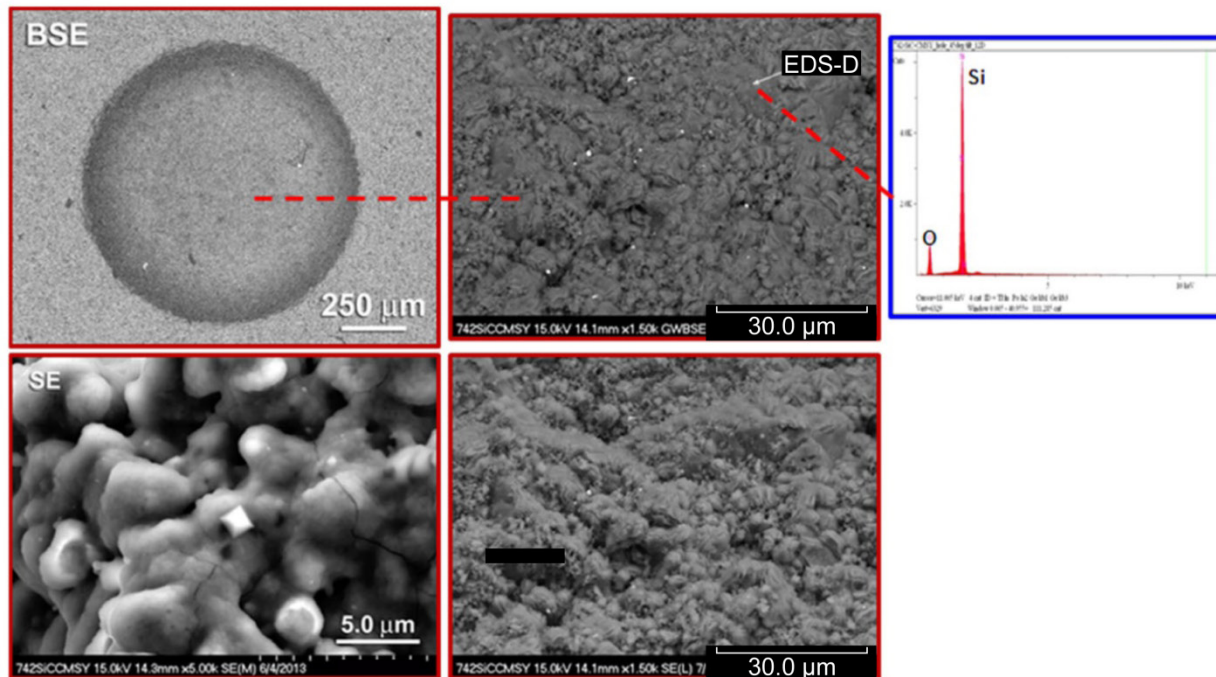


Figure 50.—Back-scattered electron images and energy dispersive spectra of the silica scale formed on 20%CrMoSiY-80%SiC after oxidation at 1700 K for a cumulative oxidation time of 100 h.

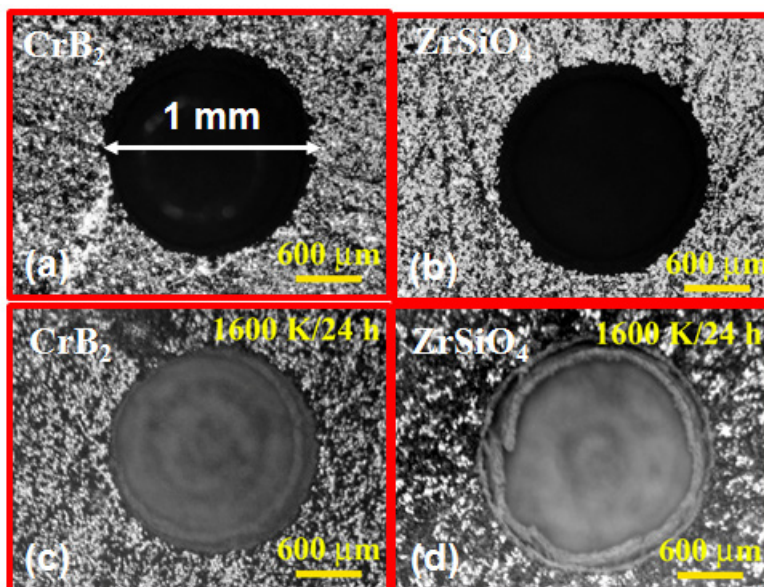


Figure 51.—Comparison of the effective of additives on the self-healing of scratches and a 1 mm diameter hole before and after oxidation at 1600 K for 24 h. (a) and (c) 20(wt.%)CrSi<sub>2</sub>-75%SiC-5%CrB<sub>2</sub>; (b) and (d) 20(wt.%)CrSi<sub>2</sub>-75%SiC-5%ZrSiO<sub>4</sub>.

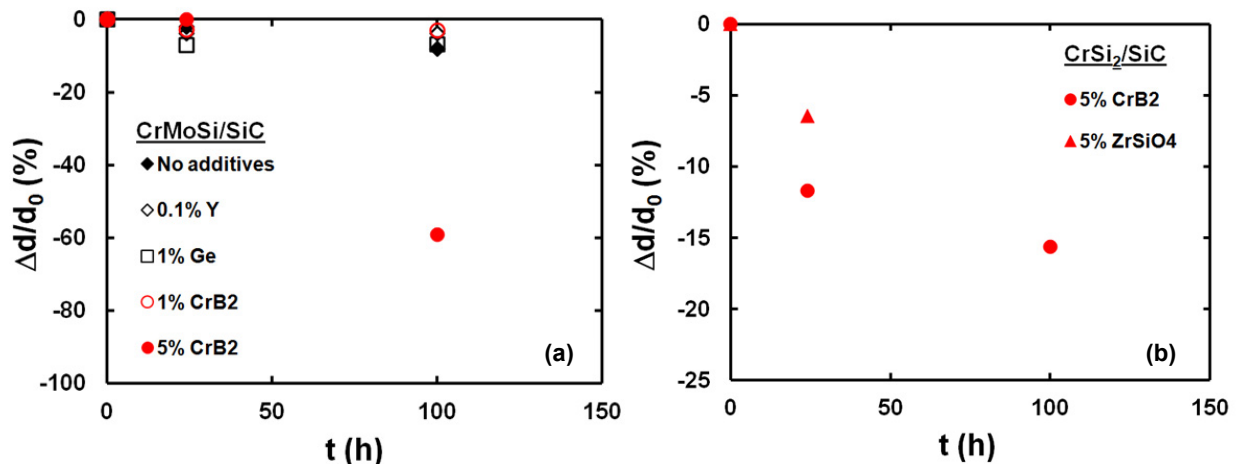


Figure 52.—Effective of self-healing additives on the relative change in the hole dimensions as a function of oxidation time. (a) CrMoSi/SiC oxidized at 1700 K; (b) CrSi<sub>2</sub>/SiC oxidized at 1600 K.

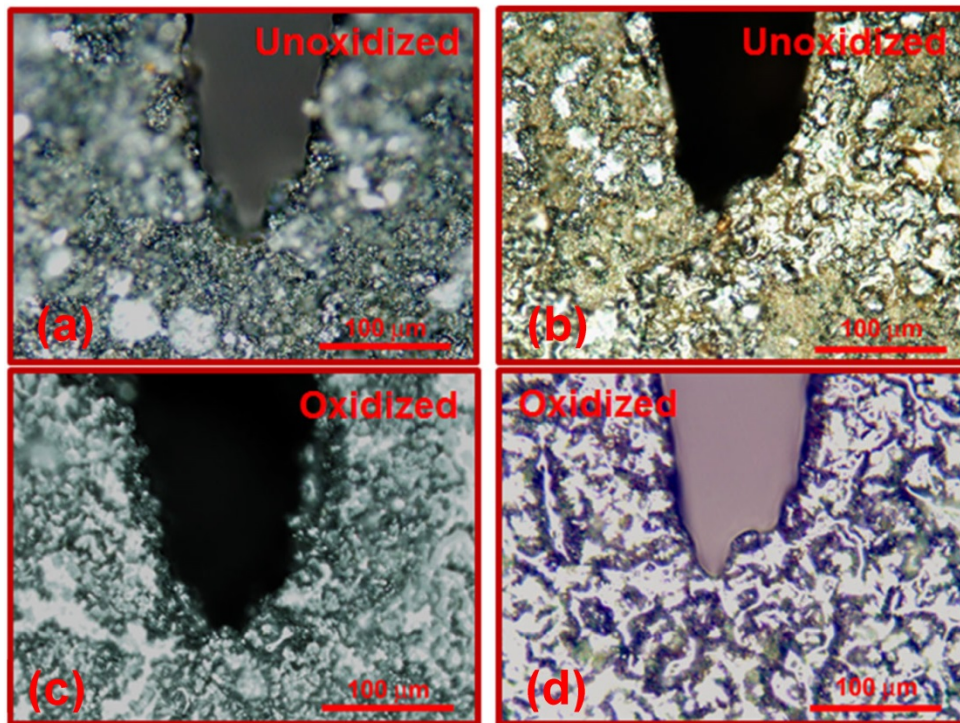


Figure 53.—Micrographs of (a) unoxidized and (c) oxidized 20(wt.%)CrMoSi-79%SiC-1%CrB<sub>2</sub> notched specimens; and (b) unoxidized and (d) oxidized 20(wt.%)CrMoSi-75%SiC-5%CrB<sub>2</sub> notched specimens. The specimens were oxidized at 1700 K for 24 h.



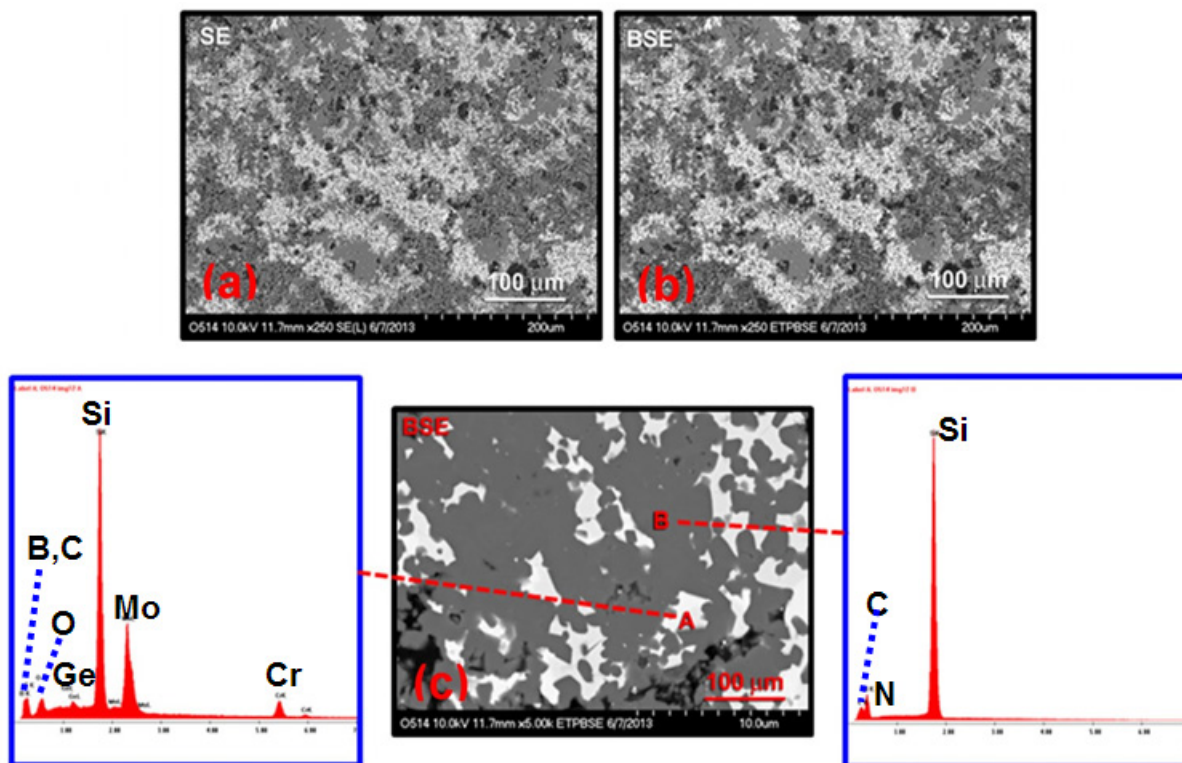


Figure 54.—(a) Secondary and (b) and (c) backscattered electron micrographs of 25(wt.%) CrMoSi-45%SiC-25%Si<sub>3</sub>N<sub>4</sub>-5%CrB<sub>2</sub> with corresponding energy dispersive spectra of the phases of a hot-pressed specimen.

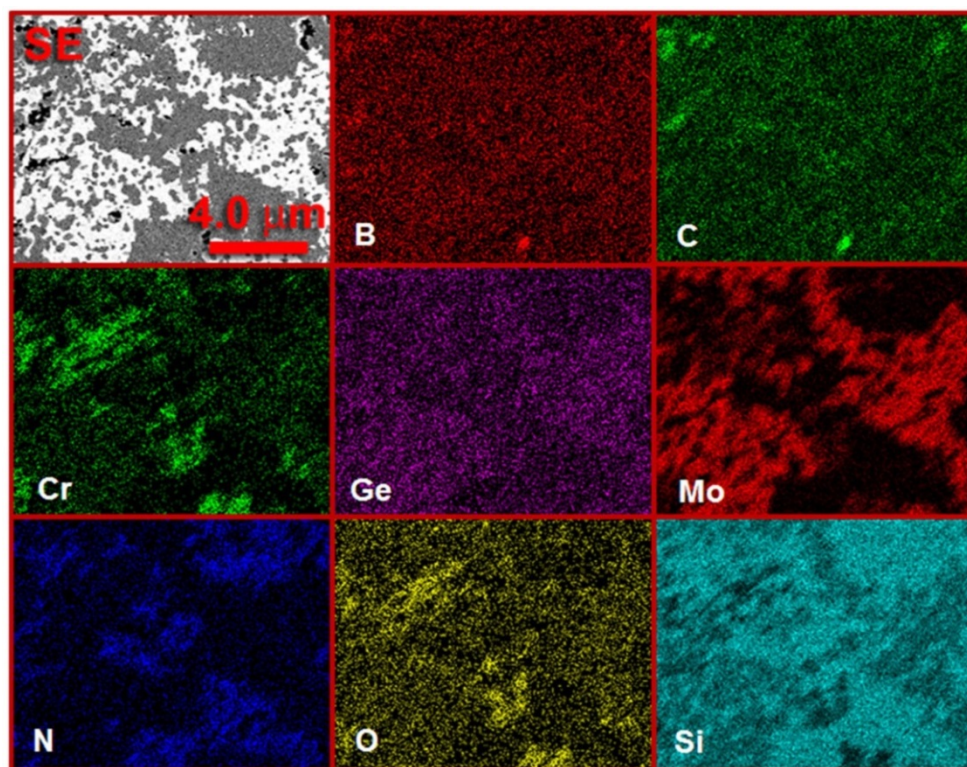


Figure 55.—Secondary electron micrograph and elemental x-ray maps of 25(wt.%) CrMoSi-45%SiC-25%Si<sub>3</sub>N<sub>4</sub>-5%CrB<sub>2</sub>.

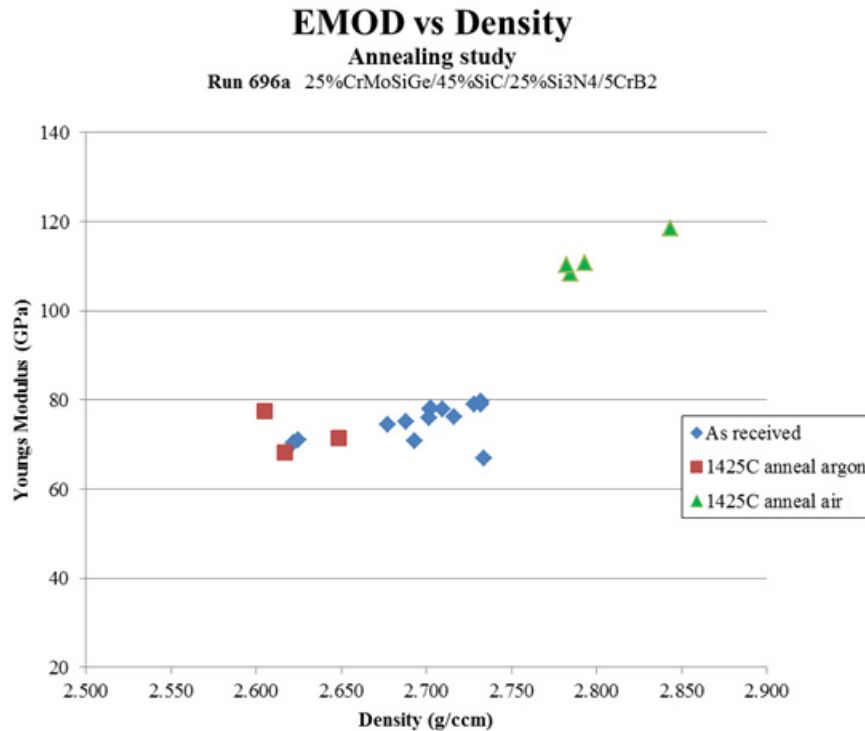


Figure 56.—Plot of Young's modulus versus density for 25(wt.%) CrMoSi-45%SiC-25%Si<sub>3</sub>N<sub>4</sub>-5%CrB<sub>2</sub> demonstrating an increase in modulus and density after annealing in air at 1498 K for 1800 s. The data for the as-received specimens and those annealed in argon under identical conditions are also included.

## 5.0 Summary and Conclusions

A concept for developing a new generation of SiC fiber reinforced engineered matrix composites is proposed for applications at 1755 K (2700 °F). The design of the engineered matrices involves several steps: Increasing the local plasticity of the matrix in a SiC/SiC composite to blunt cracks; adding additives to self-heal cracks and voids; matching the thermal expansion of the matrix with that of the SiC fibers; and minimizing the presence of unreacted silicon. Several engineered matrices containing CrSi<sub>2</sub>, a Cr-30(at.%)Mo-30%Si alloy, MoSi<sub>2</sub>, TiSi<sub>2</sub> and WSi<sub>2</sub> were designed and formulated by ball milling mixtures of the metallic silicides, SiC and Si<sub>3</sub>N<sub>4</sub> powders and hot-pressing them into desired shapes. Thermal expansion measurements of the engineered matrices were conducted to demonstrate that they matched those of SiC as proof-of-concept. The oxidation behavior of these engineered matrices were studied and based on these results, two compositions were down selected for further development. These compositions were 10(wt.%)CrSi<sub>2</sub>-70%SiC-20%Si<sub>3</sub>N<sub>4</sub> and 10(wt.%)CrMoSi-60%SiC-30%Si<sub>3</sub>N<sub>4</sub> for 1589 K (2400 °F) and 1755 K (2700 °F) applications, respectively. Four-point bend tests conducted on these engineered matrix compositions demonstrated that the bend strength increased with increasing temperature due to an increase in the local ductility of the matrix.

Having demonstrated the validity of the proposed concepts, several new engineered matrices were designed with additives to enhance their self-healing properties. Early results from self-healing studies conducted on these matrices were encouraging. It was demonstrated that additions of 5(wt.%) CrB<sub>2</sub> to CrSi<sub>2</sub>-SiC and CrMoSi-SiC matrices were effective in healing scratches and in partially closing 1 mm diameter holes. Elastic moduli measurements on a 25(wt.%) CrMoSi-45%SiC-25%Si<sub>3</sub>N<sub>4</sub>-5%CrB<sub>2</sub> SEVNB specimens showed that the Young's modulus increased when the specimens were annealed in air at 1698 K for 1800 s as compared to specimens annealed in argon. The fracture toughnesses of

specimens annealed in air and argon at 1698 K for 1800 s were measured to be 3.3 and 1.6 MPa $\sqrt{\text{m}}$ , respectively.

Attempts to fabricate engineered matrix composites by infiltrating woven preforms proved to be challenging. The engineered matrices were infiltrated into SiC/SiC woven BN and CVI SiC-coated preforms either using an aqueous or an epoxy carrier media. Despite several attempts, these efforts have been largely unsuccessful in infiltrating the preforms with sufficient loading of solids to fill at least 50 percent of the available voids ( $\sim 20$  to 25 vol.%) in the preforms. Future research will concentrate on increasing the solids loading in the preforms. A few engineered matrix composites were fabricated by particulate and melt infiltrating the preforms, where either Si or a Si-1(at.%)Ge alloy was used for melt infiltration, for fabricating specimens for bend testing. The microstructures of these composites revealed that the voids were not completely filled. Four-point bend stress-strain data on these composites obtained at room temperature and 1645 K are reported. Interestingly, the four-point bend strengths of pre-cracked and oxidized specimens at 1645 K were generally higher than the uncracked specimens.

In an attempt to develop a matrix for 1755 K with little or no unreacted silicon, melt infiltration trial runs were conducted on BN-coated Sylramic and Tyranno SA fiber preforms using CrSi<sub>2</sub> and a Cr-25(wt.%)Si alloy for melt infiltration. Thermodynamic calculations predicted that these alloys would not react with either the BN or the CVI SiC coatings. Microstructural observations of infiltrated preforms revealed that molten metal had not infiltrated large sections of the preforms. The first trial showed no evidence of any reaction between the CrSi<sub>2</sub> s and the BN and CVI SiC coatings, and Raman spectroscopy of the CrSi<sub>2</sub> matrix did not reveal the presence of C and Si. In subsequent melt infiltration trials, the microstructural evidence revealed that the CrSi<sub>2</sub> and the Cr-25(wt.%)Si had reacted with the BN and CVI SiC coatings contrary to the thermodynamic predictions. The reason for this discrepancy is unclear and it is being investigated. Developing conditions for melt infiltration with high temperature metallic silicides will be continued under the Aerosciences project. Alternative traditional methods of fabricating the composites (e.g., tape casting) will be investigated.

## References

1. T. M. Pollock and S. Tin, *J. Propulsion and Power* **22**, pp. 361-374 (2006).
2. D. Brewer, *Mater. Sci. Eng. A*, **A261**, pp. 284-291 (1999).
3. C. M. Grondahl and T. Tsuchiya, *J. Eng. Gas Turbine Power* **123**, pp. 513-519 (2000).
4. F. Christin, *Ceramic Matrix Composites* (ed. W. Krenkel), Wiley-VCH Verlag, Weinham, Germany, pp. 327-351(2008).
5. J. A. DiCarlo and N. P. Bansal, *Fabrication Routes for Continuous Fiber-Reinforced Ceramic Composites (CFCC)*, NASA TM 208819, NASA Lewis Research Center, Cleveland, OH (1998).
6. J. A. DiCarlo, H. M. Yun, G. N. Morscher and R. T. Bhatt, *SiC/SiC Composites for 1200 °C and Above*, NASA TM 213048, NASA Glenn Research Center, Cleveland, OH (2004).
7. *Handbook of Ceramic Composites* (ed. N. P. Bansal), Kluwer Academic Publishers, Boston, MA (2005).
8. *Ceramic Matrix Composites* (ed. W. Krenkel), Wiley-VCH Verlag, Weinham, Germany (2008).
9. [http://www.geaviation.com/press/other/other\\_20131114.html](http://www.geaviation.com/press/other/other_20131114.html).
10. J. Lamon, *Ceramic Matrix Composites* (ed. W. Krenkel), Wiley-VCH Verlag, Weinham, Germany, pp. 49-68 (2008).
11. G. N. Morscher and J. D. Cawley, *J. Eur. Ceram. Soc.* **22**, pp. 2777-2787 (2002).
12. G. S. Corman and K. L. Luthra, *Handbook of Ceramic Composites* (ed. N. P. Bansal), Kluwer Academic Publishers, Boston, MA, pp. 99-115 (2005).
13. J. D. Heidmann, [http://www.dtic.mil/ndia/2012physics/TuesdayHeidmann\\_Panel2.pdf](http://www.dtic.mil/ndia/2012physics/TuesdayHeidmann_Panel2.pdf).
14. [https://www.iata.org/pressroom/facts\\_figures/fact\\_sheets/pages/environment.aspx](https://www.iata.org/pressroom/facts_figures/fact_sheets/pages/environment.aspx).
15. T. L. Anderson, *Fracture Mechanics: Fundamentals and Applications* (2<sup>nd</sup> ed.), CRC Press, Boca Raton, LA, pp.343-350 (1995).



16. L. L. Fischer and G. E. Beltz, *J. Mech. Phys. Sol.* **49**, pp. 635-654 (2001).
17. S. R. Choi and V. Tikare, *Scripta Metall. Mater.* **26**, pp. 1263-1268 (1992).
18. P. Carrère and J. Lamon, *J. Eur. Ceram. Soc.* **23**, pp. 1105-1114 (2003).
19. R. Naslain, A. Guette, F. Rebillat, R. Pailler, F. Langlais and X. Bourrat, *J. Sol. State Chem.* **177**, pp. 449-456 (2004).
20. Y. S. Jung, W. Nakao, K. Takahashi, K. Ando and S. Saito, *Proc. First Intern. Conf. on Self Healing Materials*, Noordwijk aan Zee, The Netherlands, Springer (2007).
21. W. Nakao, Y. Tsutagawa, K. Takahashi and K. Ando, *Proc. First Intern. Conf. on Self Healing Materials*, Noordwijk aan Zee, The Netherlands, Springer (2007).
22. L. Quemard, F. Rebillat, A. Guette, H. Tawail, C. Louchet-Pouillier, *J. Eur. Ceram. Soc.* **27**, pp. 2085-2094 (2007).
23. L. S. Sigl, P. A. Mataga, B. J. Dalgleish, R. M. McMeeking and A. G. Evans, *Acta Metall.* **36**, pp. 945-953 (1988).
24. A. G. Evans, *J. Ceram. Soc.* **73**, pp. 187-206 (1990).
25. P. F. Becher, *J. Ceram. Soc.* **74**, pp. 255-269 (1991).
26. Y. Umakoshi, T. Nakashima, T. Nakano and E. Yanagisawa, *High Temperature Silicides and Refractory Alloys* (eds. C. L. Briant, J. J. Petrovic, B. P. Bewlay, A. K. Vasudevan and H. A. Lipsitt), **vol. 322**, Materials Research Society, Pittsburgh, PA, pp. 9-20 (1994).
27. C. A. Swenson, *J. Phys. Chem. Ref. Data*, **12**, pp. 179-182 (1983).
28. *Thermal Expansion: Nonmetallic Solids, Thermophysical Properties of Matter* (eds. Y.S. Touloukian, R. K. Kirby, R. E. Taylor and T. Y. R. Lee) **vol. 13**, Plenum, New York, pp. 1195-1220 (1977).
29. S. V. Raj, *Comparison of the Thermal Expansion Behavior of Several Intermetallic Silicide Alloys between 293 and 1523 K*, NASA-TM-2014-216678, NASA Glenn Research Center, Cleveland, OH (2014)
30. M. Hebsur, *Mater. Sci. Eng.* **A261**, pp. 24-37 (1999).
31. R. Ramachandra Rao, H. N. Roopa and T. S. Kannan, *Ceram. Intern.* **25**, pp. 223-230 (1999).
32. F. Li, H. Chen, R. Wu and B. Sun, *Mater. Sci. Eng.* **A368**, pp. 255-259 (2004),
33. J. Xiaoli, H. Hui, W. Qide, Z. Bo and S. Feng, *J. Wuhan University* **22**, pp. 754-756 (2007). DOI 10.1007/s11595-006-4754-y.
34. B. P. Singh, J. Jena, L. Besra and S. Bhattacharjee, *J. Nanoparticle Research* **9**, pp. 797-806 (2007).
35. U. Paik, V. A. Hackley and H-W. Lee, *J. Amer. Ceram. Soc.* **82**, pp. 833-840 (1999).
36. ASTM C 1421-10, *Standard Test Methods for Determination of Fracture Toughness of Advanced Ceramics at Ambient Temperature*, ASTM Refractories, Activated Carbon; Advanced Ceramics, **Vol. 15.01**, ASTM International, West Conshohocken, PA (2014).
37. S. Spinner and W. E. Tefft, *Proc. Amer. Soc. Testing Mater.* **61**, pp. 1221-1238 (1961).
38. ASTM Standard E 1876- 01 *Standard Test Method for Dynamic Young's Modulus, Shear Modulus, and Poisson's Ratio by Impulse Excitation of Vibration*, Section 3, Vol. 03.01, ASTM International, West Conshohocken, PA. pp. 1122-1137 (2004)
39. R. Schmidt, V. Wicher and R. Tilgner, *Polymer Testing* **24**, pp. 197-203 (2005).
40. S. V. Raj and A. Palczar, *Mater. Sci. Eng.*, **A 527**, pp. 2129-2135 (2010).
41. S. V. Raj, *Mater. Sci. Eng.*, **A 201**, pp. 229-241 (1995).
42. M. Hebsur, unpublished research, Glenn Research Center, Cleveland, OH (2000).
43. L. U. J. T. Ogbuji and E. J. Opila, *J. Elect. Chem. Soc.* **142**, pp. 925-930 (1995).
44. E. Liden, L. Bergström, M. Persson and R. Carlsson, *J. Eur. Ceram. Soc.* **7**, pp. 361-368 (1991).
45. C. H. McMurtry, S. K. Lau, G. V. Srinivasan and S. Chwastiak, *Silicon Carbide Reinforced Reaction Bonded Silicon Carbide Composite*, U. S. Patent 5,296,311 (1994).
46. U. Paik, H. C. Park, S. C. Choi, C. G. Ha, J. W. Kim and Y. G. Jung, *Mater. Sci. Eng.* **A334**, pp. 267-274 (2002).

47. X. Ji, H. Hao, Q. Wu, B. Zhou, F. Sun, Surface Modification of Silicon Carbide Powders, Journal of Wuhan University of Technology-Mater. Sci. Ed., Volume 22, pp 754-756 (2007). DOI 10.1007/s11595-006-4754-y.
48. A. B. Gokhale and G. J. Abbaschian, Binary Alloy Phase Diagrams, (eds. H. Okamoto, P. R. Subramanian and L. Kacprzak) **vol. 2**, pp. 1333-1335 (1990).
49. Y. Katoh, T. Nozawa and L. L. Snead, Mechanical Properties Of FCVI SiC-Matrix Composites Reinforced With Tyranno™-SA Grade-3 SiC Fiber Fabrics, ORNL report, [http://web.ornl.gov/sci/physical\\_sciences\\_directorate/mst/fusionreactor/pdf/june2005/2\\_CERAMIC/KATOH02.PDF](http://web.ornl.gov/sci/physical_sciences_directorate/mst/fusionreactor/pdf/june2005/2_CERAMIC/KATOH02.PDF), Oak Ridge, TN (2005).
50. J. A. DiCarlo and H. M. Yun, Non-oxide (Silicon Carbide) Fibers, (ed. N. P. Bansal), Kluwer Academic Publishers, Boston, MA pp. 33- 52 (2005).
51. Ube America technical literature, <http://northamerica.ube.com/content.php?pageid=54>.



